Intertidal topography mapping using the waterline method from Sentinel-1 & -2 images: The examples of Arcachon and Veys Bays in France

Edward Salameh, Frédéric Frappart, Imen Turki, Benoît B. Laignel

Version of Record: https://www.sciencedirect.com/science/article/pii/S0924271620300630
Manuscript_e2efe8b927387e83fa8dac3965ae808e

Intertidal topography mapping using the waterline method from Sentinel-1 & -2 images: the examples of Arcachon and Veys Bays in France

Edward Salameh[1,2,*], Frédéric Frappart[2], Imen Turki[1], and Benoit Laignel[1]

[1] Laboratoire Morphodynamique Continentale et Côtière (M2C), Département de Géosciences et Environnement, Université de Rouen Normandie, CNRS, Mont Saint Aignan, France.

[2] Laboratoire d'Etudes en Géophysique et Océanographie Spatiales, Université Toulouse III, CNRS, CNES, IRD, Toulouse, France

[*] Correspondence: edward.salameh@univ-rouen.fr

Intertidal flats lying as a buffer zone between land and sea provide critical services including protection against storm surges and coastal flooding. These environments are characterized by a continuous redistribution of sediment and changes in topography. Sea level rise, anthropogenic pressures, and their related stressors have a considerable impact on these areas and are expected to put them under more stress; hence the increased need for frequent and updated topography maps. Comparing to traditional surveying approaches, spaceborne remote sensing is able to provide topography maps more frequently with a lower cost and a higher coverage. The latter is currently considered as an established tool for measuring intertidal topography. In this study, an improved approach of the waterline method was developed to derive intertidal Digital Elevation Models (DEMs). The changes include a faster, more efficient and quasi-automatic detection and post-processing of waterlines. The edge detection technique consists in combining a k-means based segmentation and an active contouring procedure. This method was designed to generate closed contours in order to enable an automatization of the post-processing of the extracted waterlines. The waterlines were extracted from Sentinel-1 and Sentinel-2 images for two bays located on the French Coast: the Arcachon lagoon and the Bay of Veys. DEMs were generated for the Arcachon Bay between 2015 and 2018, and for the Bay of Veys between 2016 and 2018 using satellite acquisitions made during summer (low storm activity period). The comparison of the generated DEMs with lidar observations showed an error of about 19 to 25 cm. This study also demonstrated that the waterline method applied to Sentinel images is suitable for monitoring the morpho-sedimentary evolution in intertidal areas. By comparing the DEMs generated between 2016 and 2018, the Arcachon Bay and the Bay of Veys experienced net volume losses of 1.12×10^6 m^3 and 0.70×10^6 m^3 respectively. The generated DEMs provide useful and needed information for several scientific applications (e.g., sediment balance, hydrodynamic modelling), but also for authorities and stakeholders for coastal management and implementation of ecosystem protection policies.

Keywords: Intertidal flat; Coastal areas; Waterline; Topography; DEM; Sentinel.

1. Introduction

Intertidal flats are gently sloped areas located between the high and low water spring tide marks, inundated and exposed periodically due to the ebb and flood tides. These widely spread coastal ecosystems occur primarily in tide-dominated environments and sheltered coastal embayments (Gao, 2019). They are highly productive and diverse areas (Levin et al., 2001) that provide habitat for a large community of migratory shorebirds (Agardy and Alder, 2005), supports millions of people worldwide, stabilize the coastline, defend from storm surges, and provide protection against coastal flooding (Millennium Ecosystem Assessment,

2005; Nicholls et al., 2007). Human interventions (e.g., coastal development, land claim, dredging, upstream dams, etc.) accompanied by sea level rise due to climate change have put these regions under high pressure. A recent study conducted by Murray et al. (2019) showed that intertidal flats have declined worldwide by 16% between 1984 and 2016. A continuous monitoring of intertidal flats, especially of the intertidal topography, is thus of high ecological, economical, and societal importance. An accurate mapping of the topography in intertidal flats is fundamental for coastal flood forecasting, coastal defense, identification of shoreline erosion or accretion, navigation, fishing, economic exploitation, and tourism (Benveniste et al., 2019; Mason et al., 2010, 2000). Intertidal topography is also an essential parameter for shallow waters hydrodynamic modelling (many forcing terms in the hydrodynamic equation of motion are depth dependent, e.g. the resistance term and the wind stress) and unreliable intertidal topographies limit the accuracy of such models (Bergsma and Almar, 2018; Mason et al., 2000).

Nowadays, a wide variety of topography mapping techniques have been developed. Conventional techniques such as ground-based and airborne (e.g. stereo-photogrammetry, lidar, and Interferometric Synthetic Aperture Radar (InSAR)) surveying provide very accurate measurements of the surface elevation. Ground-based techniques are usually dedicated to small study sites, while airborne techniques can cover larger areas and inaccessible regions. However, ground- and airborne-based techniques are constrained by logistical difficulties and high costs (Mason et al., 2000). Spaceborne-based techniques provide a viable alternative for intertidal topography mapping due to their synoptic nature. The continuous monitoring that they provide enables a regular and frequent updating of the topographic maps in these highly dynamic environments.

A variety of spaceborne-based techniques for intertidal topographic mapping and DEM generation exist now (Salameh et al., 2019). The InSAR technique traditionally used for inland DEM generation has been proven to be reliable for DEM generation over intertidal areas by using images acquired at low tides. InSAR is a method with high potential for intertidal areas, but for multi-pass interferometry systems (e.g. Sentinel-1), the temporal lag between the two acquisitions with different angle is still an issue (i.e., low coherence due to long baseline, decorrelation caused by incidence angles impacting the backscattering, and changes in surface roughness from a tidal cycle to another (Choi and Kim, 2018)). This limits the use of this method to the single-pass interferometry systems for which there is no temporal decorrelation (Choi and Kim, 2018; Lee and Ryu, 2017). Catalão and Nico (2017) proposed a pixel-based algorithm to estimate intertidal topography based on the correlation between the temporal variation of pixels' backscattering coefficients and the tide height. Salameh et al. (2018) showed that satellite radar altimetry is another approach that can be used to derive topographic profiles of intertidal areas along the altimeter ground tracks. The major drawback of this technique is the inability to produce gridded-DEMs as the ground tracks coverage is not dense enough. The most common technique used for DEM generation of intertidal flats is the waterline method introduced by Mason et al. (1995). This method uses a time series of remotely sensed images acquired at different tidal stages. The waterline (shoreline) for each image is extracted and height is assigned to it using in situ or modelled sea level information. Then the waterlines are assembled and interpolated to produce a gridded-DEM. For research purposes, the waterline method proved to be one of the best methods that provides a good trade-off between technical performance (accuracy) and cost-effectiveness (Mason et al., 2000).

The waterline method was used to generate intertidal DEMs in several regions. First attempts were made over the English Coasts at the Humber/Wash area (Mason et al., 1995), the

Morecambe Bay (Mason et al., 1999), and the Holderness coast (Lohani, 1999). It was then applied for the intertidal flats of the Wadden Sea in northern Europe (Heygster et al., 2010; Li et al., 2014; Niedermeier et al., 2005), the intertidal flats of the Gomso Bay in Korea (Ryu et al., 2008), the Macouria Amazon-derived mud bank in French Guiana (Anthony et al., 2008), the Yangtze Delta (Zhao et al., 2008), and the Sea Radial Sand Ridges in the Southern Yellow Sea (Kang et al., 2017; Liu et al., 2013; Wang et al., 2019). The waterline method was also used to generate time series of DEMs to study the morphological evolution and the development of intertidal flats (Li et al., 2014; Mason et al., 2010, 1999; Ryu et al., 2008; Wang et al., 2019; Xu et al., 2016; Zhao et al., 2008).

Images acquired from radar (Synthetic Aperture Radar; SAR) and optical systems can be used by the waterline method. The major difference in terms of methodology is the edge detection techniques that can be applied to extract waterlines. SAR data are more suited for this method due to their ability to acquire images in all weather conditions, including in presence of clouds, and during day and night (Mason et al., 1999) which enables a better sampling of the tidal range. However, the edge detection (waterline extraction) for the SAR images are more problematic due to the speckle noise (Niedermeier et al., 2005). For SAR images, several approaches were implemented to extract waterlines such as the multi-scale edge detection algorithm proposed by Mason and Davenport (1996) using the Touzi edge operator (Touzi et al., 1988) combined with an active contouring model, wavelet-based edge detection methods adapted to SAR images (Heygster et al., 2010; Niedermeier et al., 2000), region based level-sets (Silveira and Heleno, 2009), and k-means clustering (Soares et al., 2012).

For generating intertidal DEMs using the waterline method, previous studies used remote sensing images acquired by a wide variety of SAR (e.g., ERS-1/2, RadarSat-1/2, EnviSat, JERS-1, COSMO-SkyMed, TerraSAR-X) (Heygster et al., 2010; Mason et al., 2010, 1999, 1995) or optical sensors (e.g., Landsat, IRS, SPOT, IKONOS, Quickbird, MOS-1) (Anthony et al., 2008; Kang et al., 2017; Ryu et al., 2008; Xu et al., 2016) while other studies used a combination of both (Li et al., 2014; Liu et al., 2013; Wang et al., 2019). The main difficulty was to obtain a sufficient number of images during a short time period (to avoid morphological changes) that covers the whole tidal range. The solution was either to increase the period of acquisition taking the risk of major morphological evolution or to use a small number of images. Nowadays, owing to the deployment of the ESA's (European Space Agency) Sentinel-1 SAR constellation (Sentinel-1A and Sentinel-1B), the revisit time over the same area can reach 2 days (Torres et al., 2012). Therefore, the acquisition period needed for sampling the whole tidal range can be highly reduced. In this study, we used Sentinel-1 images to generate digital elevation models using the waterline method. We used as well cloud-free Sentinel-2 Multi-Spectral Images (MSI) to improve the sampling of the tidal range.

Since its introduction by Mason et al. (1995), the waterline method experienced an important improvement, yet it is still not completely automatic and relies on significant manual processing. When using SAR data, noisy images must be first eliminated. This was usually done based on wind speed measurements (at the time of acquisition) by eliminating all images occurring when wind speed was higher than a fixed threshold. The disadvantages of this approach are that it relies on a threshold that should be fixed (subjectively), some useful images could be eliminated, and it can't be used in areas where no meteorological data are available. As for the methods used for extracting waterlines (edge detection techniques), they also require an eventual thresholding at some point. Due to the variant nature of remote sensing images fixing a threshold is always problematic. Furthermore, a manual post processing is performed in order to adjust the extracted waterlines and to remove intersected parts between waterlines of different levels. In the present study we aimed to achieve the

following objectives: (i) overcome the mentioned difficulties in order to reduce the manual processing and the selection of thresholds to a minimum; An edge detection technique that can be used for both Sentinel-1 (SAR) and Sentinel-2 (MSI) images was developed that allowed us to achieve the latter objective, (ii) generate intertidal DEMs using the modified waterline method for two intertidal bays located on the French Coast: the Arcachon lagoon and the Bay of Veys, (iii) estimate the accuracy of the generated DEMs using Sentinels data over the study sites, (vi) and determine the morphological changes and the associated sediment balance. It should be noted that the choice of the two study sites was motivated by the contrasted characteristics they present in order to prove the applicability of the presented methodologies in different intertidal environments. The Arcachon Bay is a sheltered lagoon with extensive muddy flats where tides enter the system through two tidal inlets while the Bay of Veys is an exposed embayment with a mix of muddy and sandy material, with abundant presence of sand.

2. Study sites

2.1. Arcachon Bay

The Arcachon Bay is a shallow, mesotidal coastal lagoon located in the southeastern part of the Bay of Biscay and connects to it through two narrow passes separated by the Arguin Bank (Figure 1.c). The tides in the bay are semi-diurnal with a weak diurnal inequality and the water exchange with the Bay of Biscay can reach up to about 384 km^3 during each tidal cycle (Plus et al., 2009). Freshwater enters the bay from rivers, canals, and groundwater. The major two tributaries are the Eyre River and the Porges Canal contributing about 73% and 24% of the total annual freshwater inputs, respectively (Plus et al., 2009). The lagoon has a total surface area of 180 km^2 with 115 km^2 corresponding to intertidal flats. The intertidal flats are drained by tidal creeks and tidal channels with a maximum depth around 20 m (Deborde et al., 2008). They are composed of a mix of muddy and sandy material, and a large area (70 km^2) of the flats are vegetated by Zostera noltii seagrass (Blanchet et al., 2005; Proença et al., 2019).

2.2. Bay of Veys

The Bay of Veys is a shallow estuarine embayment located in the southern shore of the English Channel, in the western part of the Bay of Seine (Figure 1.b). The bay receives freshwater input from several coastal streams and four main rivers: the Aure, the Douve, the Taute, and the Vire, draining a catchment area of 3500 km^2 (Grangeré et al., 2009; Lafforgue et al., 2018). The Vire is the largest river flowing directly into the bay and provides 40% of the freshwater input (Grangeré et al., 2009). It should be noted that the main four rivers flow into the bay through sluice gates that open at ebb tide and close at flood tide (Lafforgue et al., 2018). The bay is located in a semidiurnal macrotidal environment with a tidal range that reaches 8 m at spring tides (Grangeré et al., 2009). At low tides, the surface of the uncovered intertidal flats is about 37 km^2 (Grangeré et al., 2009; Timsit et al., 2004). These flats extend to 5 km offshore. The lower part is devoid of vegetation and covered by muddy and sandy sediments, while the upper part near the land is colonized by halophytic species dominated by *Spartina anglica* (Deroin, 2012; Timsit et al., 2004). The bay is surrounded by polders protected by dikes (Deroin, 2012). The intertidal area can be separated into three major parts: the central part bounded by Carentan Channel (the Douve and the Taute confluence) from the west and by Isigny-Sur-Mer Channel (the Vire and the Aure confluence) from the east, and the eastern and western flanks.

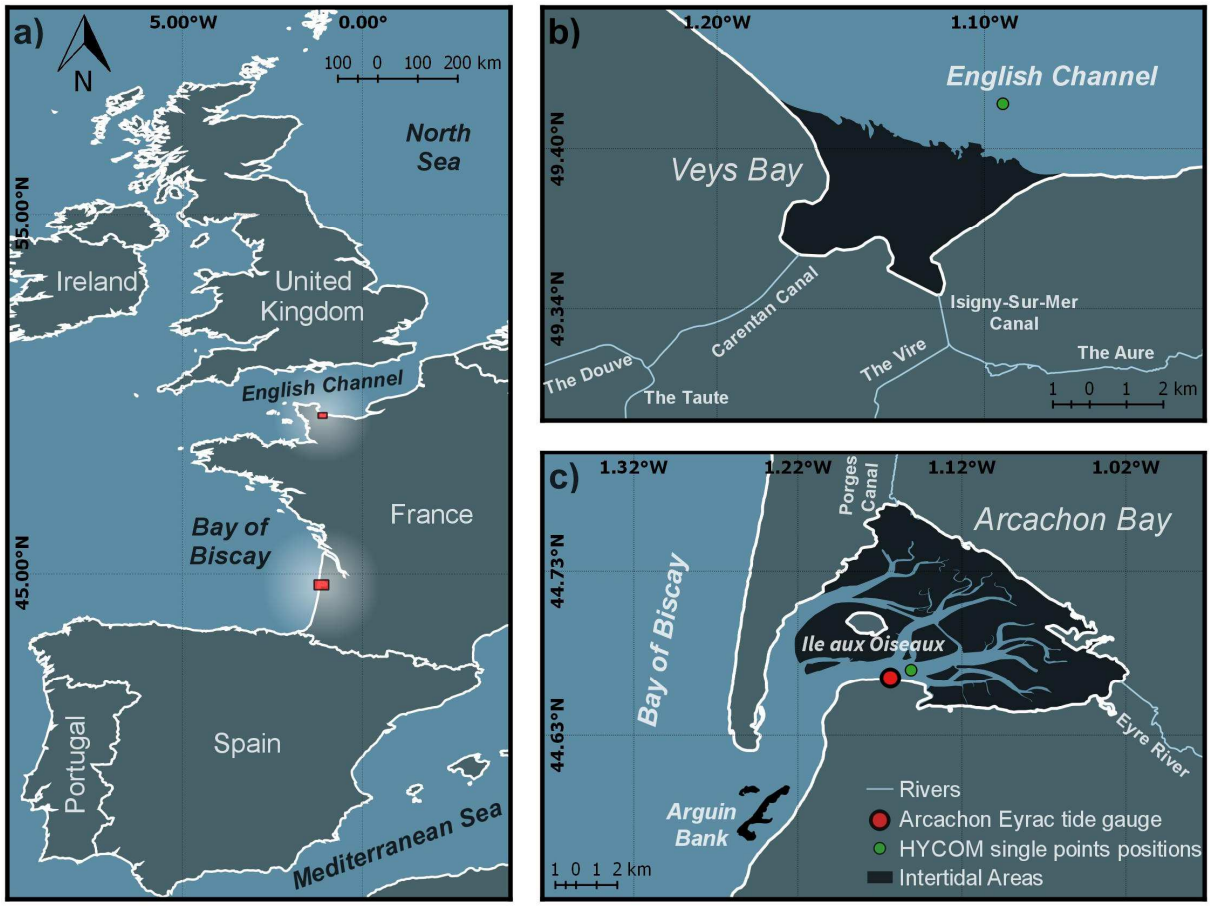

Figure 1. (a) An overview map with the location of the study sites: (b) the Arcachon Bay and (c) the Bay of Veys. (b) and (c) include the intertidal flats and the rivers and canals flowing into the two bays.

3. Datasets

Three different types of data were used in this study. Satellite images were used to extract the waterlines, tide gauge and ocean-circulation model output to determine the height (elevation) of the extracted waterlines, and lidar-derived DEMs to validate the DEMs generated by the waterline method.

3.1. Sentinel-1 and Sentinel-2 satellite images

ESA is currently putting into orbit the Sentinel satellite series as part of the Copernicus program (formerly known as the Global Monitoring for Environment and Security (GMES) program) (Showstack, 2014)developed for a long-term monitoring of the Earth surface (ocean, land, ice caps) and of its surrounding environment (atmosphere) at high spatial and temporal resolutions to provide high quality information for scientific and operational purposes (Malenovský et al., 2012).

Sentinel-1 mission is a two-satellite constellation (Sentinel-1A and Sentinel-1B) with the same reference orbit (Torres et al., 2012). Sentinel-1A and -1B were respectively launched on 3 April 2014 and on 25 April 2016. Each of the Sentinel-1 satellites orbit at an altitude of 693 km, on a near polar sun-synchronous orbit, an inclination of 98.18°, and a local solar time of 18:00 at its ascending node with 12-day repeat cycle (Torres et al., 2012). The major interest of this constellation composed of two satellites put in a 180-degree phase difference is to increase the temporal coverage (Torres et al., 2012). Owing to this configuration, the revisit time is at least six days and can reach 4 and even 2 days between two satellite acquisitions with increasing

latitudes and especially over high priority areas such as Europe, Canada and the Northern Atlantic region (ESA, 2013; Torres et al., 2012). The following information has been extracted from Fletcher (2012). The main payload instrument onboard Sentinel-1A and Sentinel-1B is a C-band Synthetic Aperture Radar (SAR) called C-SAR, operating at a frequency of 5.405 GHz. Sentinel-1 operates in 4 modes: Interferometric Wide-swath mode (IW), Extra Wide-swath mode (EW), Wave mode (WV), and Strip Map mode (SM). IW, EW, WV, and SM modes acquire data with ground resolutions of 5 m × 20 m, 20 m × 40 m, 5 m × 5 m, and 5 m × 5 m respectively. Slant range, Single-Look Complex (SLC) and Ground Range, Multi-Look, Detected (GRD) level-1 products are generated in the four acquisition modes. The SLC products consist of complex images containing amplitude and phase information. For the GRD products, SAR data are multi-looked to reduce speckle noise at the expense of spatial resolution. It should be noted that for GRD products the phase information is lost.

The data used in this study are GRD products acquired in IW mode with VV polarization. The GRD products are used in full resolution with a ground resolution of 23 m × 23 m and pixel spacing of 10 m × 10 m in range × azimuth. In this study, the GRD products were chosen instead of SLC products because they are more convenient for automatic edge detection due to their reduced speckle noise and their smaller volume of data. The merged sub-swaths are also more suited for reducing the processing time. The VV polarization was used rather than the other available VH polarization because of the better contrast obtained using the former polarization.

Sentinel-2 mission is also a two-satellite constellation (Sentinel-2A and Sentinel-2B) acquiring multi-spectral observations in 13 spectral bands. Sentinel-2A and -2B were respectively launched on 23 June 2015 and on 7 March 2017. They both orbit on a Sun-synchronous quasi-polar orbit with a 10-day repeat cycle each (5-day with 2 satellites at the equator resulting in 2-3 days at mid-latitudes) (Drusch et al., 2012). The following information has been extracted from the Sentinel-2 user handbook (ESA, 2015). The average orbital altitude is 786 km with an inclination of 98.62°, and a 10:30 a.m. descending node. It provides observations over land and coastal areas from 56° latitude South to 84° latitude North. The main payload on-board Sentinel-2 satellite is a Multi Spectral Instrument (MSI) measuring the radiance reflected by the Earth in 13 spectral bands in the visible (VIS), the near infra-red (NIR), and the short-wave infra-red (SWIR). The data are acquired on a wide swath of 290 km width with 4 bands at 10 m of spatial resolution, 6 bands at 20 m of spatial resolution, and 3 bands at 60 m of spatial resolution. Two data products are made available: the level-1C Top-Of-Atmosphere (TOA) geocoded reflectance and the level-2A Bottom-Of-Atmosphere (BOA) geocoded reflectance. Both products are composed of tiles of 100 km × 100 km ortho-images in UTM/WGS84 with 10, 20, and 60 m of spatial resolution depending on the spectral band. For edge detection purposes both products showed similar performances. The level-1C product was used in this study because of its smaller data volume.

3.2. Sea Level information from Arcachon-Eyrac tide gauge and the HYCOM ocean-circulation model

Sea level records from the Arcachon-Eyrac tide gauge (1° 9’ 48.78’’ W, 44° 39’ 54.003’’) were used in this study. The tide gauge is operating since November 1967 and managed by the French hydrographic service (Service Hydrographique et océanographique de la Marine (SHOM)) and the Gironde sea and land state office (Direction Départementale des Territoires et de la Mer (DDTM)). Since February 2010, the tide gauge is equipped with an Optiwave 7300C sensor and a MARELTA acquisition unit (REFMAR, 2012). Sea level measurements are provided (in meter) as time series of 1-minute interval given in UTC (Coordinated Universal

Time) and referenced to the French chart vertical datum. The data are made available by REFMAR and can be found online on the SHOM data website: https://data.shom.fr.

The sea level (tide and surge) model outputs from the HYbrid Coordinate Ocean Model (HYCOM) (Bleck, 2002), in barotropic configuration (Baraille and Filatoff, 1995), with a curvilinear grid and a resolution that ranges between 2 km and 500 m when approaching the French coast were also used over our two study sites. This ocean circulation model is a joint effort between the SHOM and Météo-France in the framework of the HOMONIM (History, Observation and Modeling of sea level) project, that aims to improve the coastal flood warning system in metropolitan France and overseas (SHOM, 2016). It is forced by tides predicted by the SHOM and by wind and atmospheric pressure obtained from Météo-France meteorological models (Pasquet et al., 2014). Different configurations of this model exist depending on the geographic domain of the region. In this study we used the data obtained by the ATL (Atlantic) configuration that covers the French Atlantic façade and the English Channel between 43°N 9°W and 62°N 10°E. At high surge the model underestimates the total sea level of about 10 cm with a phase difference of about 12 minutes (Pasquet et al., 2014). Archived hourly forecasts (unit: m) of sea level (tide and surge referenced to the Mean Sea Level) over Arcachon and Veys Bays were provided by SHOM at https://data.shom.fr. These forecasts were interpolated to a 1-minute interval.

The lidar-derived DEMs used in this study (presented in the next subsection) for the Arcachon Bay and the Bay of Veys are referenced to the NGF/IGN69 (French reference system) vertical datum. For comparison purposes, and in order to generate waterline-derived DEMs referenced to the same vertical datum, water level elevations extracted from the tide gauge and from the ocean circulation model were converted to the NGF/IGN69 vertical datum. Originally tide gauge and HYCOM water levels were referenced to the French chart and to the Mean Sea Level respectively. Vertical datum conversions were made using information provided by the French hydrography service (SHOM) data website (data.shom.fr) giving the vertical differences between the different datums throughout the French coast.

3.3. Lidar-derived topography for intertidal areas

A lidar-derived topography of the intertidal area of the Arcachon Bay is a subset of the RGE ALTI® product provided by the national institute for geography and forest information (IGN) at http://professionnels.ign.fr/rgealti. Airborne lidar acquisitions were acquired on 25 June 2013 at low tide. The dataset is provided on a regular 1 × 1 m grid and interpolated on a 10 × 10 m grid (Figure 2.a). The vertical precision for this dataset is 0.2 m.

The validation topography for the Bay of Veys was also derived from an airborne lidar acquisitions. The intertidal topography of the bay was extracted from the NHDF (lidar Normandie Hauts-De-France) 2016-2017 V.20180501 product provided by the SHOM (SHOM-ROLNP, 2018). The data were acquired during campaigns conducted from 5 May 2017 to 26 June 2017 and led by the SHOM in partnership with the Normand Picard Coastal Observation Network (ROLNP – Réseau d'Observation du Littoral Normand Picard). The product provides Digital Elevation Models (DEMs) of 1 × 1 m and 5 × 5 m resolutions. In this study the 5 × 5 m DEM was used after interpolation on a 10 × 10 m grid (Figure 2.b). Arcachon and Veys lidar-derived DEMs were resampled (using the bilinear interpolation technique) to the 10 × 10 m grid used for the generated waterline-derived DEMs in order to compare the two types of DEMs.

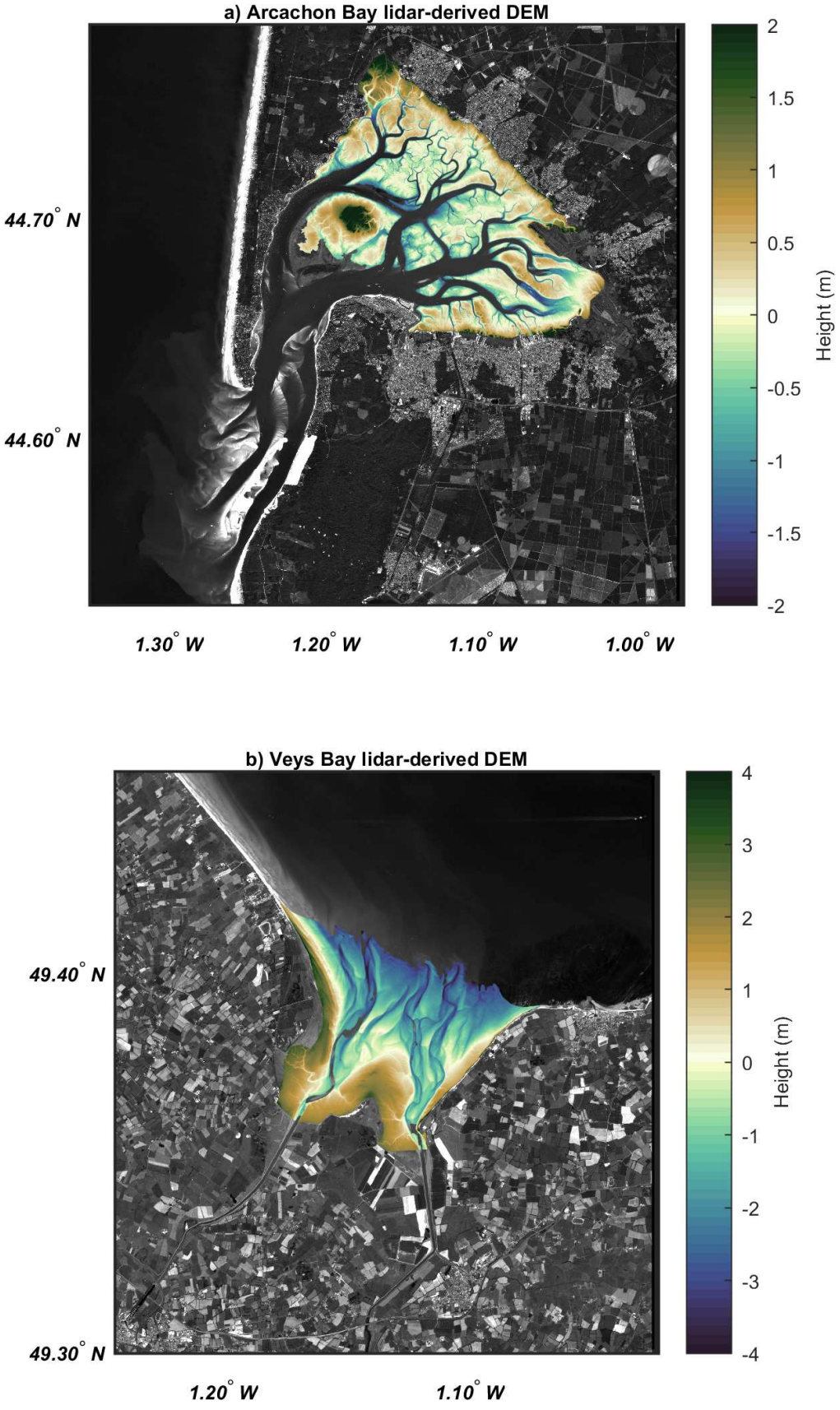

Figure 2. Lidar-derived DEMs used for validation for the (a) Arcachon Bay (extracted from the RGE ALTI® product provided by the national institute for geography and forest information (IGN)) and (b) the Bay of Veys (extracted from the NHDF (lidar Normandie Hauts-De-France) 2016-2017 V.20180501 product provided by the SHOM (Shom-ROLNP, 2018)). Heights are referenced to the French Reference System NGF/IGN69 datum.

4. Methods

In this study, the DEMs were generated using the waterline method. A detailed description of this method can be found in Mason et al. (1995) and Heygster et al. (2010). Before applying the waterline method on the Sentinel-1 and Sentinel-2 data, a pre-processing step was performed first to produce filtered backscattering coefficient images from Sentinel-1 scenes and Normalized Difference Water Index (NDWI) images from Sentinel-2 scenes. The aim of the pre-processing steps is to enhance the contrast of the images in order to detect the edges of the tidal flats. In this section, the pre-processing of Sentinel data using SNAP (SentiNel Application Platform) software (ESA, 2018) is presented first, then a detailed summary of the waterline method is given along with the changes applied in this study. Figure 3 presents a flowchart that exhibits the different steps of the methodology along with their corresponding sections.

4.1. SNAP pre-processing

Sentinel-1 SAR and Sentinel-2 MSI images were pre-processed using the SNAP toolbox. The pre-processing workflows were designed using the SNAP graph builder tool. For SAR images, the pre-processing workflow consisted of four steps to obtain the geo-corrected backscatter images: (i) thermal noise removal using the "Thermal Noise Removal" operator of SNAP Sentinel-1 ToolBoX (S1TBX) that removes the thermal noise calculated by the operational ESA Instrument Processing Facility (IPF) (Bourbigot et al., 2016) and stored in a Look Up Table (LUT) within the Sentinel-1 Level-1 products (Weiß, 2019), (ii) calibration to derive radar backscattering coefficient (σ_0) values (Miranda and Meadows, 2015); this process convert the radar reflectivity stored as Digital Numbers (DN) in Sentinel-1 Level-1 products to backscattering coefficients, (iii) speckle-filtering using Refined Lee filtering (Lee, 1981), and (iv) orthorectification using the range Doppler terrain correction operator with SRTM 3" DEM (Small and Schubert, 2008).

For the multispectral images, the workflow consisted of the three following steps: (i) resampling of the different spectral bands to 10 m using a bilinear interpolation method, (ii) computation of the Normalized Difference Water Index (NDWI) (McFeeters, 1996); NDWI is defined as:

$$NDWI = \frac{\rho_{green} - \rho_{NIR}}{\rho_{green} + \rho_{NIR}}$$

where ρ_{green} and ρ_{NIR} are the reflectances of the green and the Near Infra-Red (NIR) bands; For Sentinel-2 images spectral bands 3 and 8 were respectively used for the green and NIR bands, and (iii) reprojection of pixels into WGS84 Coordinated Reference System (CRS).

4.2. Elimination of noisy SAR images

Prior to edge detection, noisy SAR images must be eliminated in order to extract only accurate waterlines. In this study, we opted for an automatic elimination of noisy images to reduce the manual interventions. The elimination was based on information extracted from the histograms of SAR images. By examining the histograms of the images, we noticed that the histograms can be divided into 6 classes. An automatic classification of the images was performed using the k-means algorithm based on the following steps: (i) histograms of 1000 bins were generated for each image, (ii) then each bin was considered as a dimension for the k-means clustering. Figure 4 shows the averaged histograms obtained for each class. Histograms showing approximately one peak (class 5 and class 6) are noisy images with low contrast between different surface types. SAR images corresponding to these classes (5 and 6) are

eliminated from further processing. Figure 5 shows two examples of SAR images corresponding to class 5 and class 6 respectively.

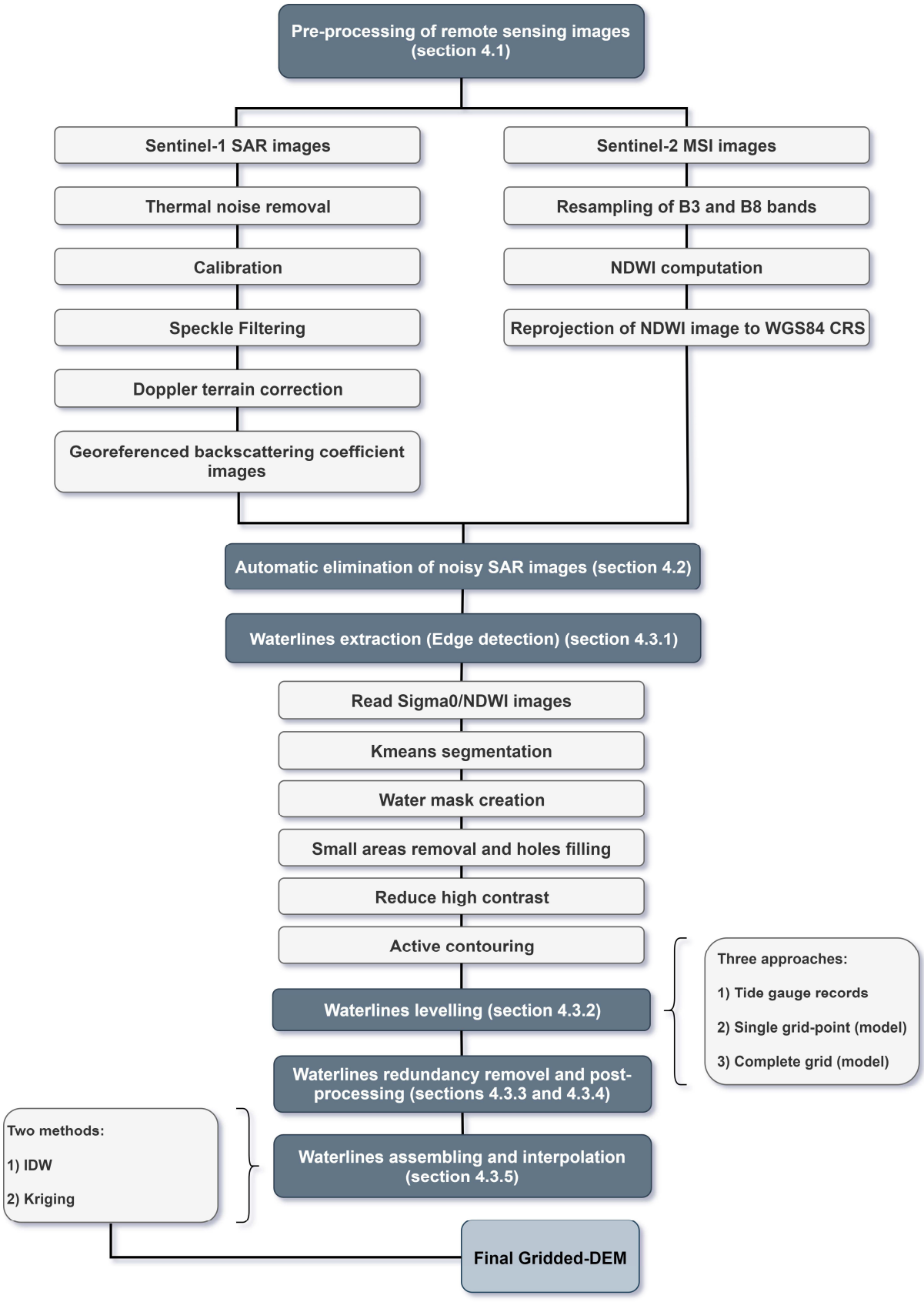

Figure 3. A step by step overview of the methods used in this study to generate Digital Elevation Models (DEMs) using the waterline method along with the corresponding sections.

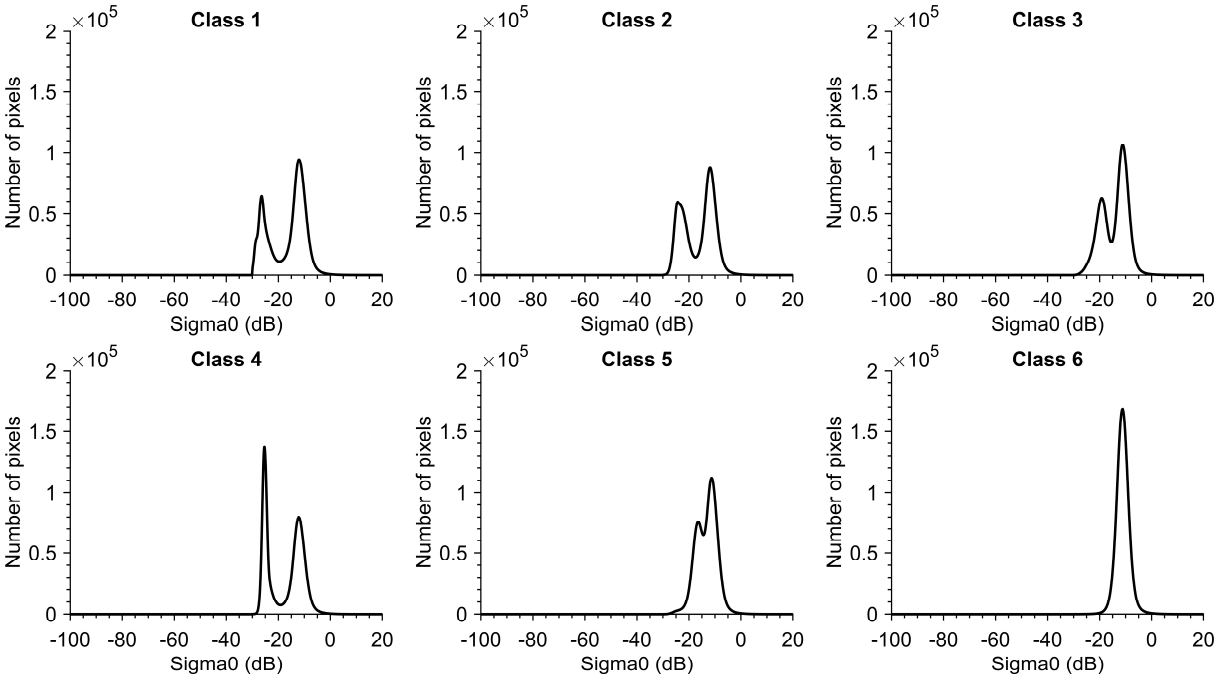

Figure 4. Averaged histograms of each class obtained by classifying the images' histograms using k-means algorithm.

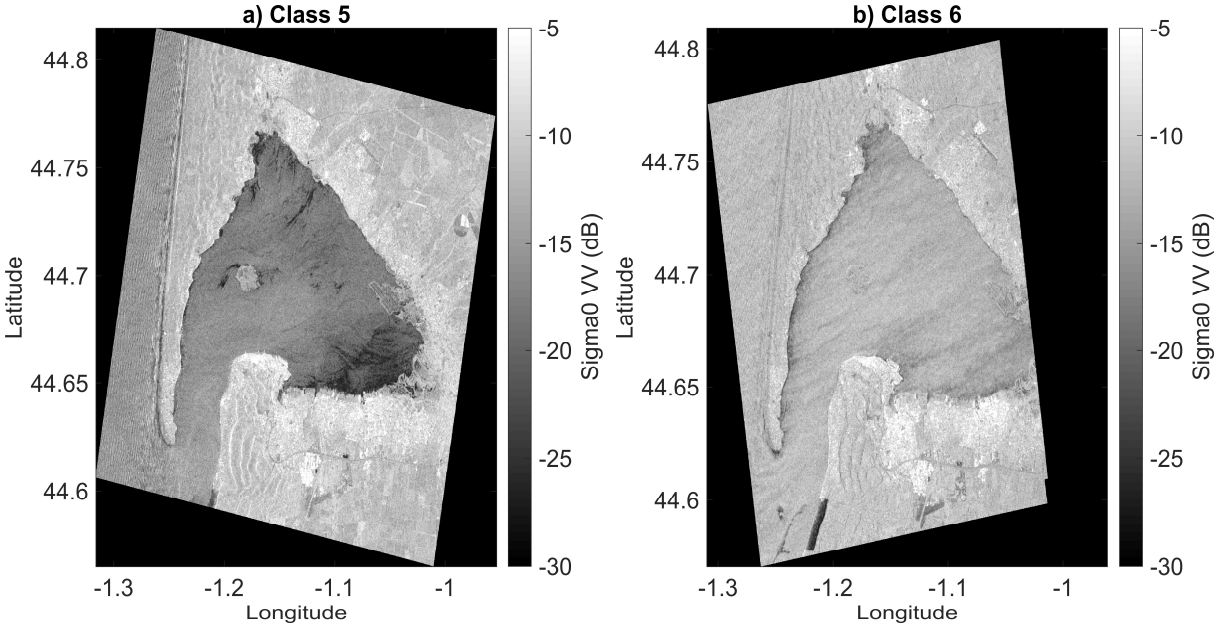

Figure 5. Examples of noisy SAR images acquired over the Arcachon Bay with histograms corresponding to: a) class 5 and b) class 6.

4.3. Waterline method

The method consists in detecting the waterline (shoreline) edge of remotely sensed images using image processing techniques. Then heights are assigned to waterlines using water level information obtained either by using a hydrodynamic tide/surge model outputs over the observed area at the time of acquisition of the image or by tide gauge measurements (Mason

et al., 1995). From a series of images providing an adequate sampling of the tidal range, a set of waterlines is assembled and then interpolated to form a gridded-DEM.

4.3.1. Edge detection

An edge detection method was developed to extract waterlines from Sentinel-1 (SAR) and Sentinel-2 (MSI) images. The method can be divided into eight steps described below and illustrated in Figure 6 using the Sentinel-1B SAR image acquired the 04/07/2017 as an example:

1) Pre-processing of Sentinel-1 & -2 images using the SNAP toolbox as explained in section 4.1 to obtain backscattering coefficient or NDWI images (Figure 6.a).
2) Performing the image segmentation process using k-means clustering technique (Arthur and Vassilvitskii, 2007). The image is divided into three different groups of pixels depending on their backscattering coefficient or NDWI values (Figure 6.b). For SAR images, open water surfaces exhibit low backscattering coefficients than other features due to the lack of penetration of the electromagnetic wave in the water, the side looking geometry of the sensor, and the smoothness of the surface responsible for low power return to the sensor. Therefore, the group with the lowest centroid is composed of the pixels corresponding to water. The other groups correspond to tidal flats or inland areas. For MSI images, the pixels corresponding to water are the pixels of the group with the highest centroid (high NDWI values correspond to water).
3) Isolating the water pixels by merging the pixels of the other groups together which will produce a water mask (Figure 6.c).
4) Extracting the perimeter of the water mask as an initial k-means-derived edge (Figure 6.d).
5) Removing small areas that usually corresponds to noisy features (Figure 6.e)
6) Filling holes that correspond to sediments, with backscattering coefficients close to the water pixel values, or to water ponds unconnected to the water of the bay for which elevation cannot be assigned using sea level information (Figure 6.f).
7) Preparing the original image to the active contouring step. In this step, the pixels of the groups with the third centroid value are replaced by the centroid value of the second group. This will turn off (reduce high backscattering coefficients) the highly energetic pixels that may attract the edge towards them in the final active contouring step (Figure 6.g).
8) Active contouring (Chan and Vese, 2001) applied on the modified image to obtain the final edge (Figure 6.h)

The edge detection method was developed in order to extract waterlines in the form of continuous and closed polygons (or many polygons for a waterline). The purpose behind this approach is to enable the automatization of the post-processing of waterlines, more specifically in removing redundant waterlines (section 4.3.3) and in removing the intersections between the different waterlines prior to interpolation (section 4.3.4).

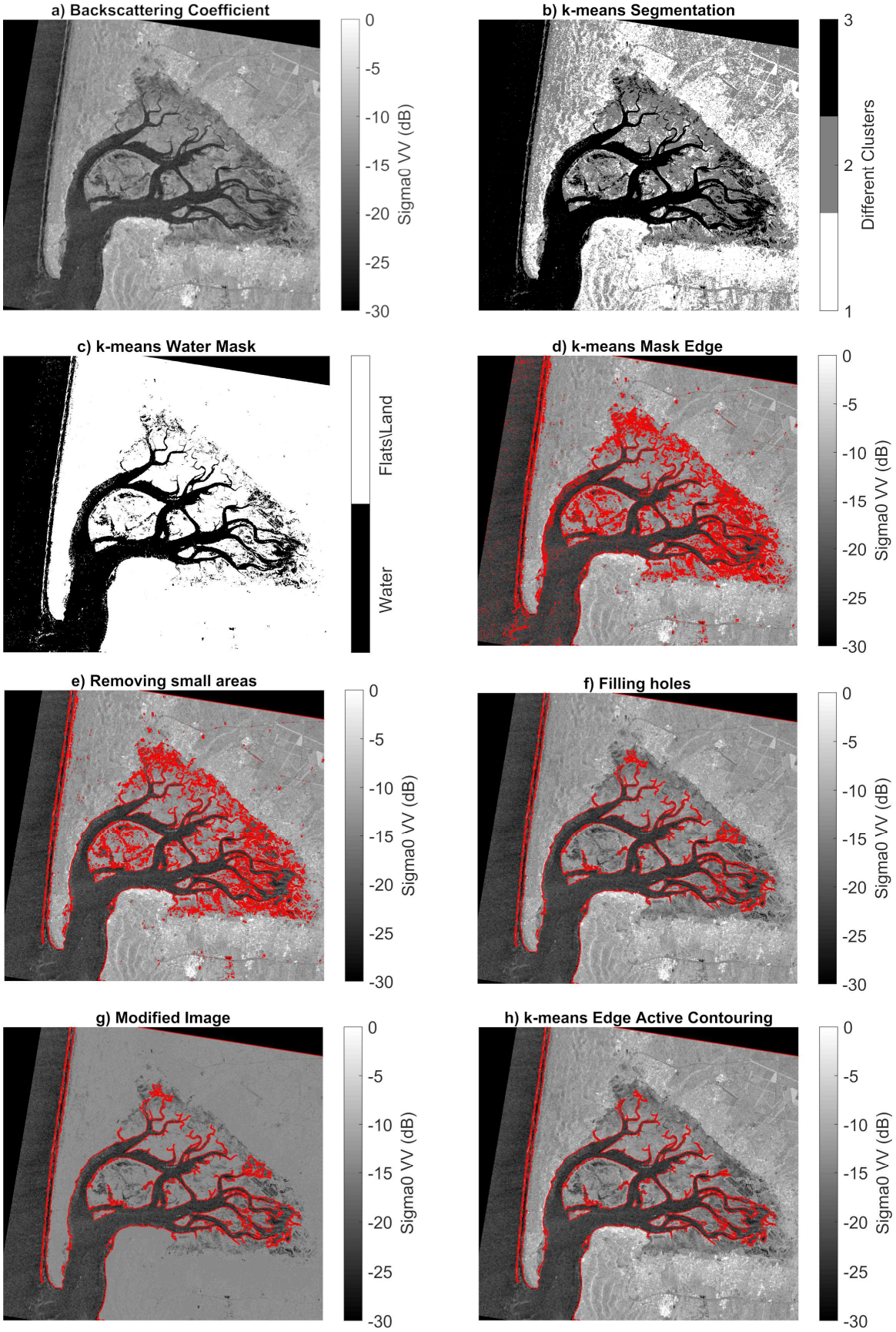

Figure 6. The different steps of the edge detection technique that combines a k-means segmentation process with a snake active edge contouring algorithm.

4.3.2. Determination of waterlines heights

In this step, heights are associated to the extracted waterlines from water level information. As mentioned in the datasets section, water level information comes from either tide gauge records (Arcachon-Eyrac in the case of the Arcachon Bay) or from the SHOM operational sea level ocean-circulation model outputs. For the Arcachon Bay, DEMs were created based on waterlines with heights extracted from the tide gauge. The water level assigned to each waterline was the closest measurement made within 1-minute interval of the satellite passage (otherwise the waterlines were discarded). DEMs were also created for the Arcachon Bay using the model simulation outputs by considering the time series of the nearest model grid-point to the tide gauge for comparison purposes. This comparison provided a quality-check of the simulated data inside the bay, in order to use the model simulations for the Bay of Veys where no tide gauge measurements are available. For the Bay of Veys sea level time series were extracted from a grid-point at the mouth of the Bay. Assembling all the waterlines produced DEM point clouds that will be interpolated on a grid of 10 × 10 m resolution.

In reality, each waterline has a range of heights. This range is not taken into consideration when using a single sea level height measurement. The assumption made is that the surface water slope is negligible which can be the case. To account for surface water slopes, DEMs over the Arcachon and Veys Bays were also generated from waterlines with heights extracted from the whole water level grid-points provided by the simulations over the study areas. The height was assigned to each point of the waterlines according to the closest water level point.

Thus, the waterlines extracted from satellite images were levelled using three different approaches:

1. Tide gauge: By assigning the water level extracted at the exact time of the satellite passage, from the tide gauge sea level times series.
2. Model (single point): By assigning the water level extracted at the exact time of the satellite passage, from a single point-grid of the ocean-circulation model outputs. The location of the single grid-points for Arcachon and Veys Bays are shown in Figure 1.
3. Model (complete grid): By assigning to each point of the waterline the water level extracted at the exact time of the satellite passage, from the closest point-grid of the ocean circulation model.

4.3.3 Redundancy removal

The redundancy removal consists in eliminating waterlines with very close heights. Due to the abundance of images provided by the Sentinel missions, many redundant waterlines were present. For instance, in a range of 15 cm, 1 to 6 waterlines can be found. For each 15 cm interval, one waterline is considered to be enough. The choice of 15 cm is arbitrary and larger intervals could be used if the number of images is low. As mentioned in sub-section 4.2, the edge detection technique allowed to extract each waterline as closed polygons (or objects). This step permits to automatically choose the waterline by keeping in each 15 cm interval the waterline with the least number of objects. For different waterlines with very similar heights, the waterline with the least number of objects is the waterline that corresponds to the image with the least noisy features. Figure 7 shows an example of three images in a 15 cm range that have different number of objects. Image number 2 possessing the least number of objects is the one which was kept for further processing. This step allows a second-degree removal of intermediate-quality images presenting some noisy features, that were not eliminated in the elimination process (section 4.2).

4.3.4. Waterlines post-processing

Waterlines with different heights may intersect due to the variable quality of images that impact the edge detection process or, less likely, due to changes in topography between the acquisitions of the images. The extraction of waterlines as closed polygonal regions, thanks to the edge detection method used, helps with the automatic removal of these intersections. For each waterline, its intersections with all the previous higher waterlines were identified then removed.

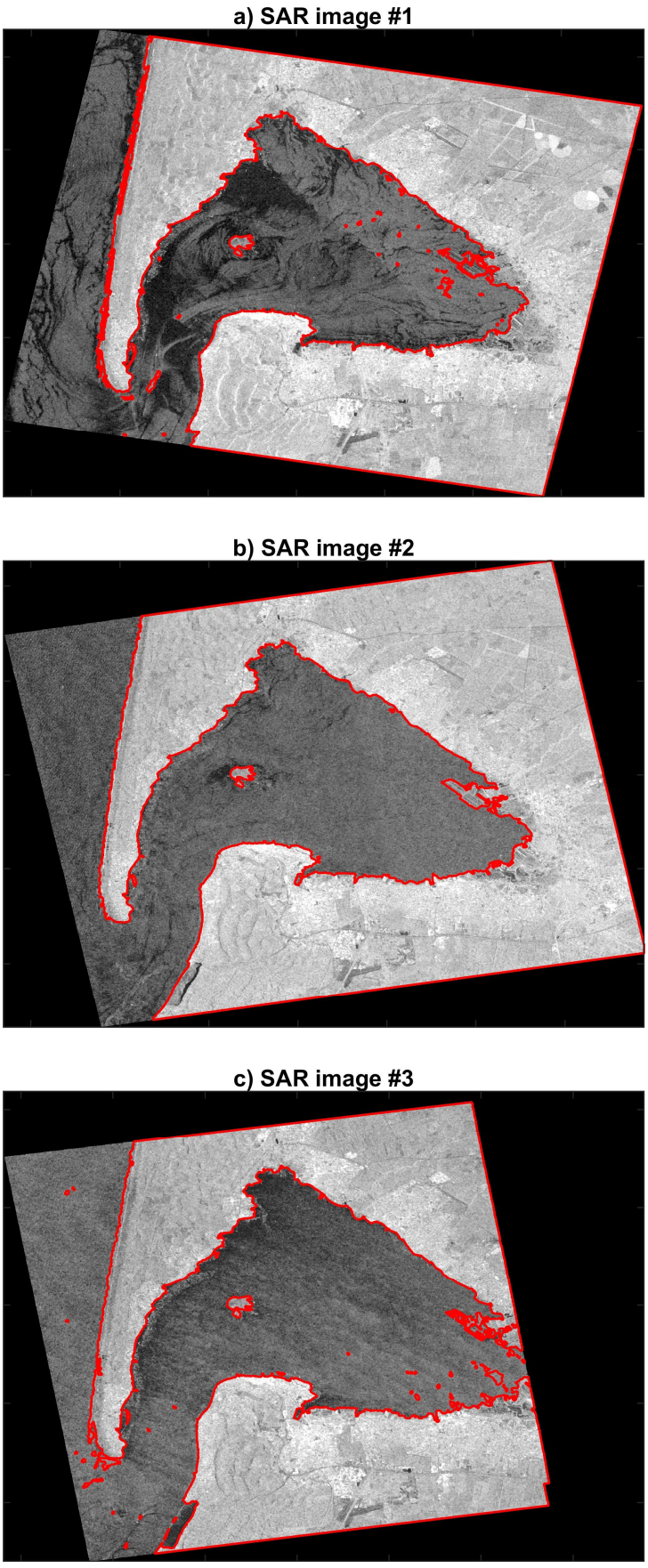

Figure 7. Examples of redundant waterlines with quasi-same height and different number of polygons. Waterline #2 presents the least number of polygons.

4.3.5. Interpolation

The DEM point clouds were then interpolated to obtain continuous gridded-DEMs. In this study two interpolation methods widely used in geo-statistics were employed and compared: Inverse Distance Weighting (IDW) (Shepard, 1968) and kriging (Matheron, 1963). The point cloud was interpolated on grids of 10-meter resolution covering the study area. Kriging was performed using the Gstat software (Pebesma, 2004; Pebesma and Wesseling, 1998).

4.4. Topographic changes

Topographic changes were analyzed by subtracting the waterline-derived DEMs (creating DEM of Difference (DoD) maps) of simultaneous years. The inherent uncertainty of the generated DEMs considerably affects the estimation of the volume changes. In order to detect real changes, we adopted the approach introduced by several studies (Brasington et al., 2000; Lane et al., 2003; Wheaton et al., 2009) that consists in specifying a Level of Detection (LoD) threshold. Absolute differences lower than this threshold will be excluded as they are considered as measurement errors rather than actual changes. The uncertainty of the DoD (δ_d) can be estimated by standard independent error propagation (Brasington et al., 2000):

$$\delta_d = \sqrt{(\delta h_{DEM1})^2 + (\delta h_{DEM2})^2}$$

where δh_{DEM1} and δh_{DEM2} are the uncertainties of the DEMs used for DoD generation. The *LoD* can be computed using the following equation (Schimel et al., 2015):

$$LoD(k) = k.\delta_d$$

where *k* is a dimensionless threshold factor. In this study, we opted for *k = 1* that corresponds to a confidence level of 68%. An estimation of the uncertainty of the waterline-generated DEMs is presented in section 5.3. After the determination of the *LoD*, the eroded and deposited volumes were computed using the following equations:

$$V_{eroded} = \sum_i [h_2(i) - h_1(i) < \quad -LoD].R^2$$

$$V_{deposited} = \sum_i [h_2(i) - h_1(i) > \quad LoD].R^2$$

where *i* denotes a grid cell, h_1 and h_2 are heights corresponding to the first and second DEMs, and *R* is the DEM resolution (R^2 is the surface of a grid cell). The volumetric uncertainties are computed with the following equations:

$$\delta V_{eroded} = R^2.\delta_d.n_{[h_2(i)-h_1(i)<-LoD]}$$

$$\delta V_{deposited} = R^2.\delta_d.n_{[h_2(i)-h_1(i)>LoD]}$$

where n is the number of grid cells presenting erosion or deposition. Finally, the net volume change is given by the sum of the eroded and deposited volumes:

$$V_{net} = V_{eroded} + V_{deposited}$$

5. Results

DEMs were generated for the Arcachon Bay and the Bay of Veys using the waterline method that can be summarized by the following steps: (i) extracting the waterlines from a series of remote sensing images that provide an adequate sampling of the tidal range, (ii) associating heights to the points of each waterline using water level information simulated or observed at

the exact time of the satellite passage, (iii) assembling all the waterlines to form a point cloud DEM, (iv) and interpolating the point cloud to construct the final gridded-DEM.

Sentinel-1 and Sentinel-2 images were used to create the DEMs. Annual DEMs were generated every year from 2015 to 2018 for the Arcachon Bay, and every year from 2016 to 2018 for the Bay of Veys. The images time series used for each DEM were acquired between the first of June and the end of September. Limiting the images to the latter calm season will help us avoid the eventual major morphological changes that could occur during a more dynamic period. Table 1 lists the number of Sentinel-1 and Sentinel-2 images acquired for each year during the June-September period for both study sites, and the number of images eliminated due to unavailable sea level information, noisy images, and redundant waterlines heights. Heights were associated to waterlines following the three different approaches mentioned earlier in the method section: (i) using the tide gauge records, (ii) using the sea level values extracted from a single point-grid of the ocean-circulation model outputs, (iii) and using the sea level distribution over the study areas from the gridded model outputs (each waterline point is given the height of its closest grid-point in space and at the exact time of satellite passage). Finally, the assembled waterlines (DEM point clouds) were interpolated using the IDW and the kriging interpolation techniques.

In the following, we will first present the method validation performed by comparing the waterline generated DEMs to the lidar-derived DEMs. Then, we will show the final intertidal DEMs obtained by the waterline method followed by an estimation of the DEMs accuracy. Finally, volume changes between the observed years will be computed from the DoD maps.

Table 1. The number of available Sentinel-1 and Sentinel-2 images for Arcachon and Veys Bays between 2015 and 2018 and the number of eliminated images due to unavailable sea level information, noisy (SAR) or cloudy (MSI) images, and images with redundant water level.

Study Site	Year	Mission	Number of available images	Number of eliminated images due to:		
				Unavailable sea level information	Noisy/cloudy images	Redundant water level
Arcachon	2015	Sentinel-1	36	1	9	11
		Sentinel-2	0	0	0	0
	2016	Sentinel-1	37	3	9	13
		Sentinel-2	5	0	0	0
	2017	Sentinel-1	79	3	20	38
		Sentinel-2	6	0	1	0
	2018	Sentinel-1	87	15	26	32
		Sentinel-2	13	4	0	0
Veys	2016	Sentinel-1	24	0	13	2
		Sentinel-2	2	0	0	0
	2017	Sentinel-1	58	0	34	7
		Sentinel-2	4	0	0	0
	2018	Sentinel-1	49	0	33	10
		Sentinel-2	13	0	1	0

5.1. DEMs validation

Figure 8 presents the comparisons for the Arcachon Bay between the lidar-derived DEM and the 2016 six waterline-derived DEMs obtained by combining the three waterlines levelling approaches with the two interpolation techniques. Another aim of this comparison is to evaluate the best combination of levelling approach and interpolation technique. For this reason, the DEMs of 2016 were chosen instead of 2015 (closer to the lidar acquisitions) for which no model simulation was performed by the SHOM. As indicated in Figure 8, the kriging interpolation method (Figure 8.b, 8.d, and 8.f) produced slightly more accurate DEMs than IDW

method (Figure 8.a, 8.c, and 8.e) showing a lower Mean Absolute Error (MAE) and a lower Root Mean Square Error (RMSE) for all cases. Tide gauge levelling showed better results (MAE = 0.19 m) than the two other approaches based on the model simulations. However, reliable DEMs were also obtained for the latter cases with MAEs and RMSEs equal to 0.25 m and ±0.32 m respectively. In contrary to expectations, the DEMs with heights assigned using the complete model grid produced the same results as the DEMs with heights assigned using the single-grid point.

The comparisons corresponding to the Bay of Veys are presented in Figure 9. DEMs of 2017 were used in this case since the lidar observations were acquired between May and June 2017. The interpretations made for the Arcachon Bay DEMs are valid for the Bay of Veys. A decrease in the MAEs and RMSEs is observed between the two interpolation techniques.

The final DEMs were thus generated using the kriging interpolation method with heights assigned using tide gauge records for the Arcachon Bay and using the kriging interpolation method and heights assigned with the single-grid point model for the Bay of Veys. Figure 10.a and 10.b show respectively, the absolute difference between the 2013 lidar-derived DEM and the 2016 waterline-derived DEMs for Arcachon Bay (tide gauge levelling and kriging interpolation), and the absolute difference between the 2017 lidar-derived DEM and the 2017 waterline-derived DEM for Bay of Veys (single-grid point model levelling and kriging interpolation).

5.2. Intertidal DEMs

The assembled waterlines used for generating the gridded DEMs are shown in Figure 11. Figure 12 shows the generated DEMs for the Arcachon Bay. The four DEMs reflect a good correspondence with the lidar-derived DEM (Figure 2.a). The relatively large features of the intertidal zone are well detected. These large features are stable in time, which is consistent with the sedimentary characteristics of the Arcachon Bay (Allard et al., 2009). Some smaller features that can be found in a given DEM are sometimes missed in others. This depends on the temporal sampling of the tidal range. For instance, the 2018 DEM shows more details than the 2015 DEM, smaller tidal flat features and tidal creeks were detected. This was majorly due to the finer sampling provided by the Sentinels in 2018 where the four satellites (S1A, S1B, S2A, and S2B) were in orbit. Despite the better sampling for the years 2017 and 2018, the detection of the very small tidal creeks was limited by the sensor horizontal resolution. A simple visual comparison between the lidar-derived DEM and the waterline-derived DEMs shows that the latter features are not detected or not fully detected by the waterline method over the Arcachon Bay. It should be noted that the DEMs were interpolated over the intertidal area specified by an intertidal mask. This mask was created manually according to the satellite image acquired at the lowest tide (-1.53 m) during the 2018 June-September period. The DEMs of the other years may present some errors near the intertidal area's borders due to a missing waterline. This can be well observed for the DEM of 2015 for which the lowest waterline was extracted at -0.78 m.

The DEMs generated for the Bay of Veys are presented in Figure 13. The topography shape and height are consistent with the lidar-derived DEM. Figure 13 shows a net improvement with time in terms of details. The tidal creeks in the 2018 DEM are evident comparing to the DEM generated for 2016. The 2017 DEM shows an intermediate performance.

5.3. DEMs accuracy

The accuracy of the generated DEMs is governed by the following factors: (i) horizontal resolution of the remote sensing images (sensor-dependent), (ii) the geometric corrections, (iii)

horizontal accuracy of the edge detection technique, (iv) the slope of the intertidal zone topography, (v) the accuracy of sea level information, and (vi) the slope of the surface water. The first three factors are related to horizontal inaccuracies that will lead to a height (vertical) uncertainty depending on the fourth factor. These three factors are also sensor-dependent, and their inaccuracies are determined by the SAR images since they have the lower spatial resolution (23 m x 23 m). The accuracy of the geometric corrections of the SAR images is within one pixel, therefore a horizontal uncertainty of 23 m. The edge detection technique (taking into account the speckle filtering) yielded an uncertainty of 2 pixels in the shoreline positions, therefore an uncertainty of 46 m. The latter was determined by a visual assessment of detected waterlines. The average intertidal slope obtained from the lidar-derived DEMs for the Arcachon Bay and the Bay of Veys are 0.17 % and 0.13 %, respectively. This results in a height error of 0.12 m (23*0.17/100 + 46*0.17/100) for Arcachon and 0.09 m (23*0.13/100 + 46*0.13/100) for the Bay of Veys. The fifth and sixth factors have a direct impact on the height accuracy. The combined uncertainties coming from the tide gauge and the slope for the case of Arcachon and from the model and the slope for the Veys Bay don't exceed 0.15 m. The uncertainty is thus 0.27 m (0.12 + 0.15) for Arcachon Bay and 0.24 m (0.09 + 0.15) for the Bay of Veys. These uncertainties are considered as conservative, and they are close to the observed MAEs. The estimated uncertainties allow an estimation of δ_d (same as the *LoD* by taking $k = 1$) for both study sites: 0.38 m for Arcachon Bay and 0.34 m for the Bay of Veys.

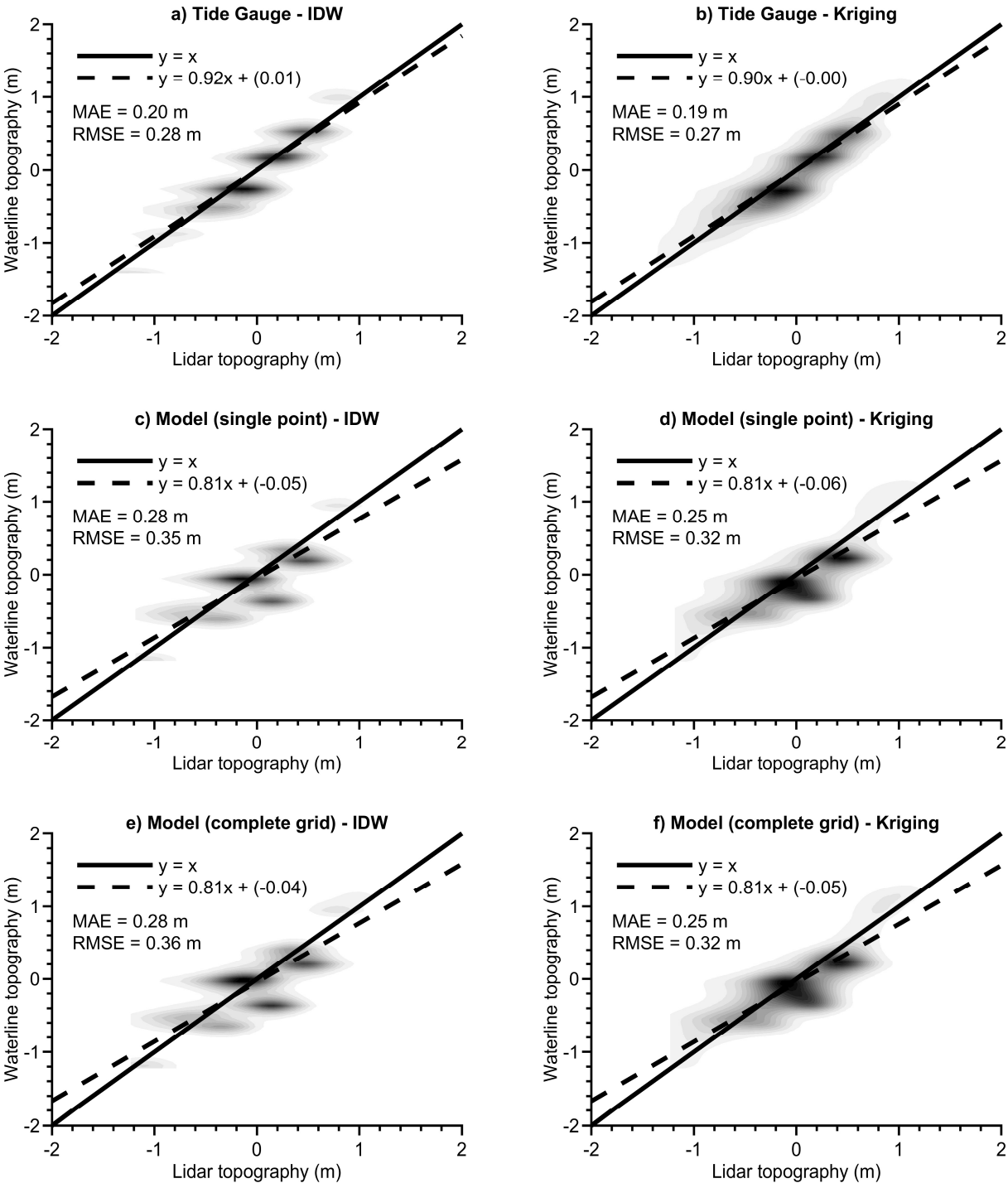

Figure 8. Comparisons between the lidar-derived DEM and the 2016 waterline-derived DEMs for the Arcachon Bay generated using: (a) IDW interpolation and tide gauge levelling; (b) kriging interpolation and tide gauge levelling; (c) IDW interpolation and single point model levelling; (d) kriging interpolation and single point model levelling; (e) IDW interpolation and complete grid model levelling; (f) kriging interpolation and complete grid model levelling.

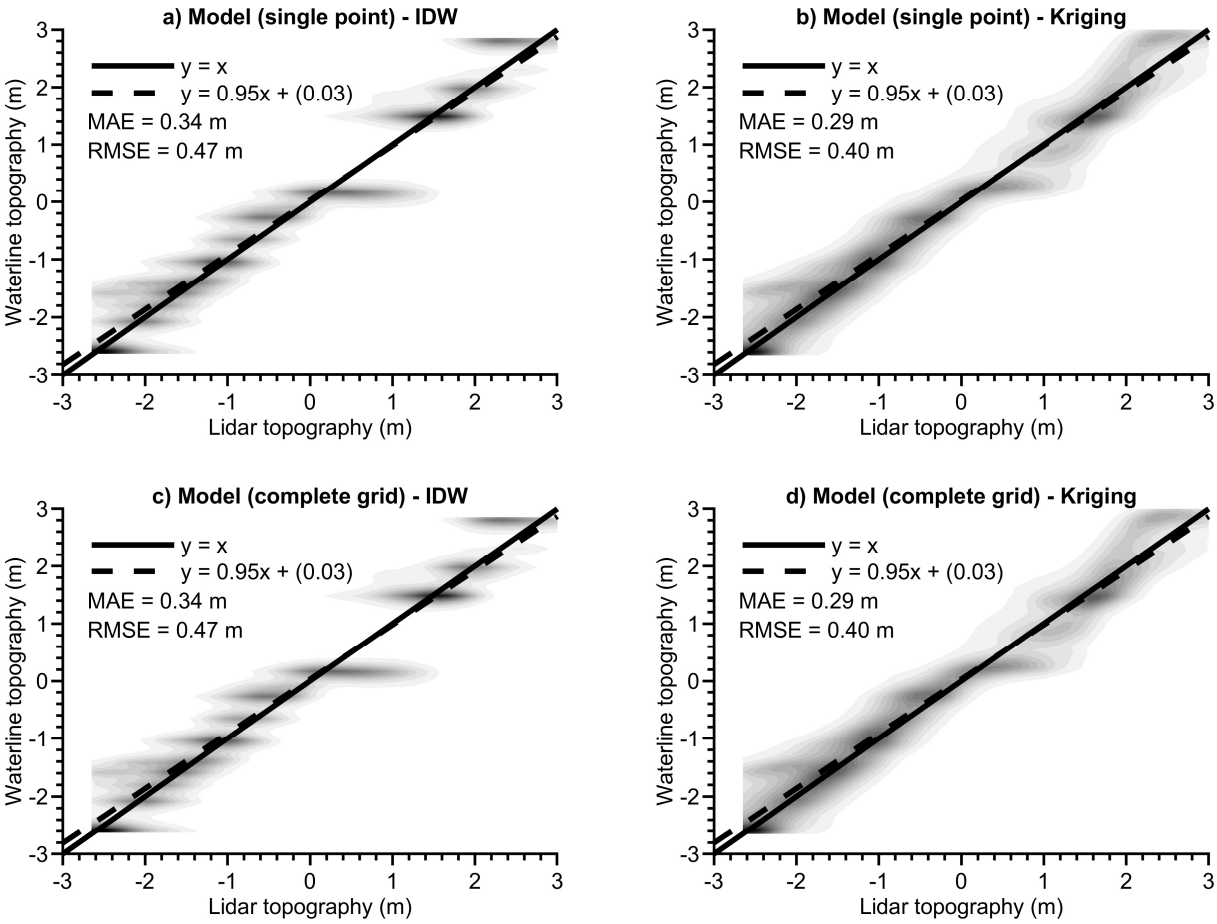

Figure 9. Comparisons between the lidar-derived DEM and the 2017 waterline-derived DEMs for the Veys Bay generated using: (a) IDW interpolation and single point model levelling; (b) kriging interpolation and single point model levelling; (c) IDW interpolation and complete grid model levelling; (d) kriging interpolation and complete grid model levelling.

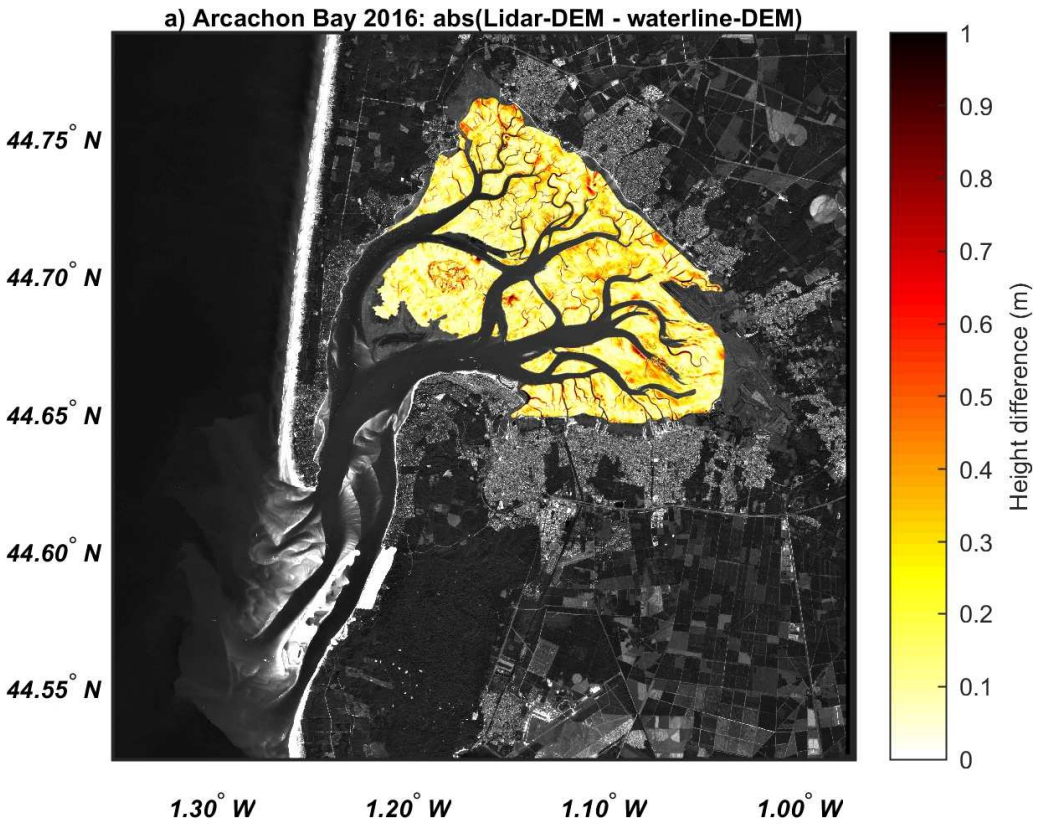

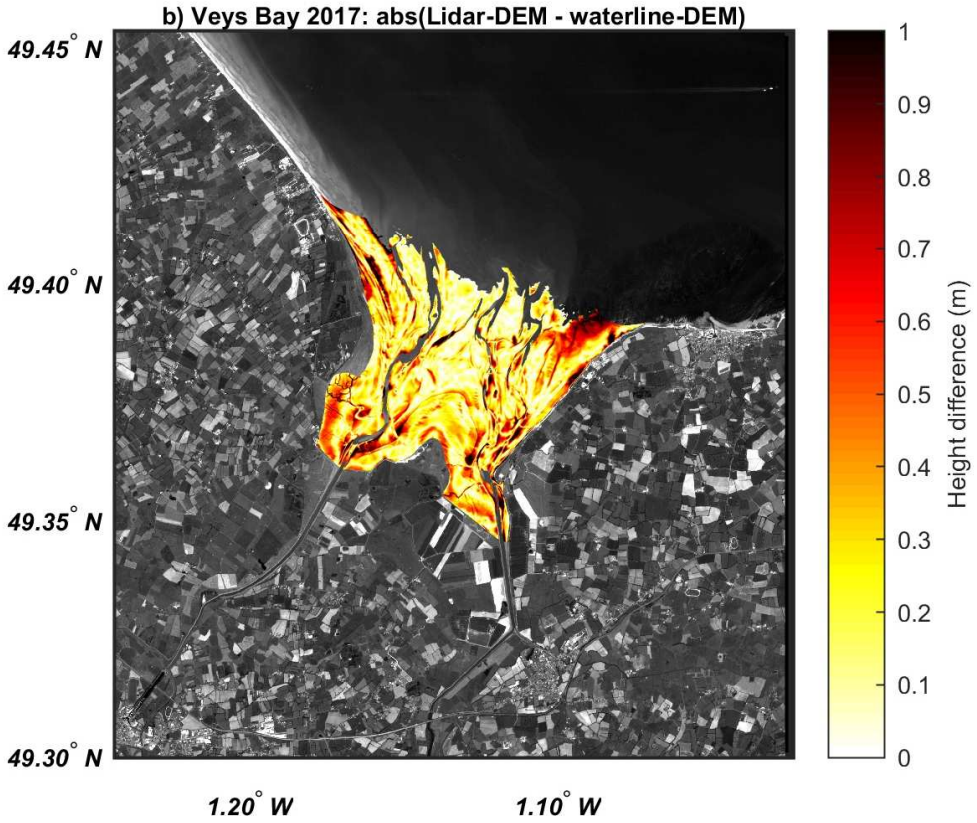

Figure 10. Absolute difference between a) Arcachon lidar-derived DEM (2013) and the 2016 waterline-derived DEM; b) Veys Bay lidar-derived DEM (2017) and the 2017 waterline-derived DEM.

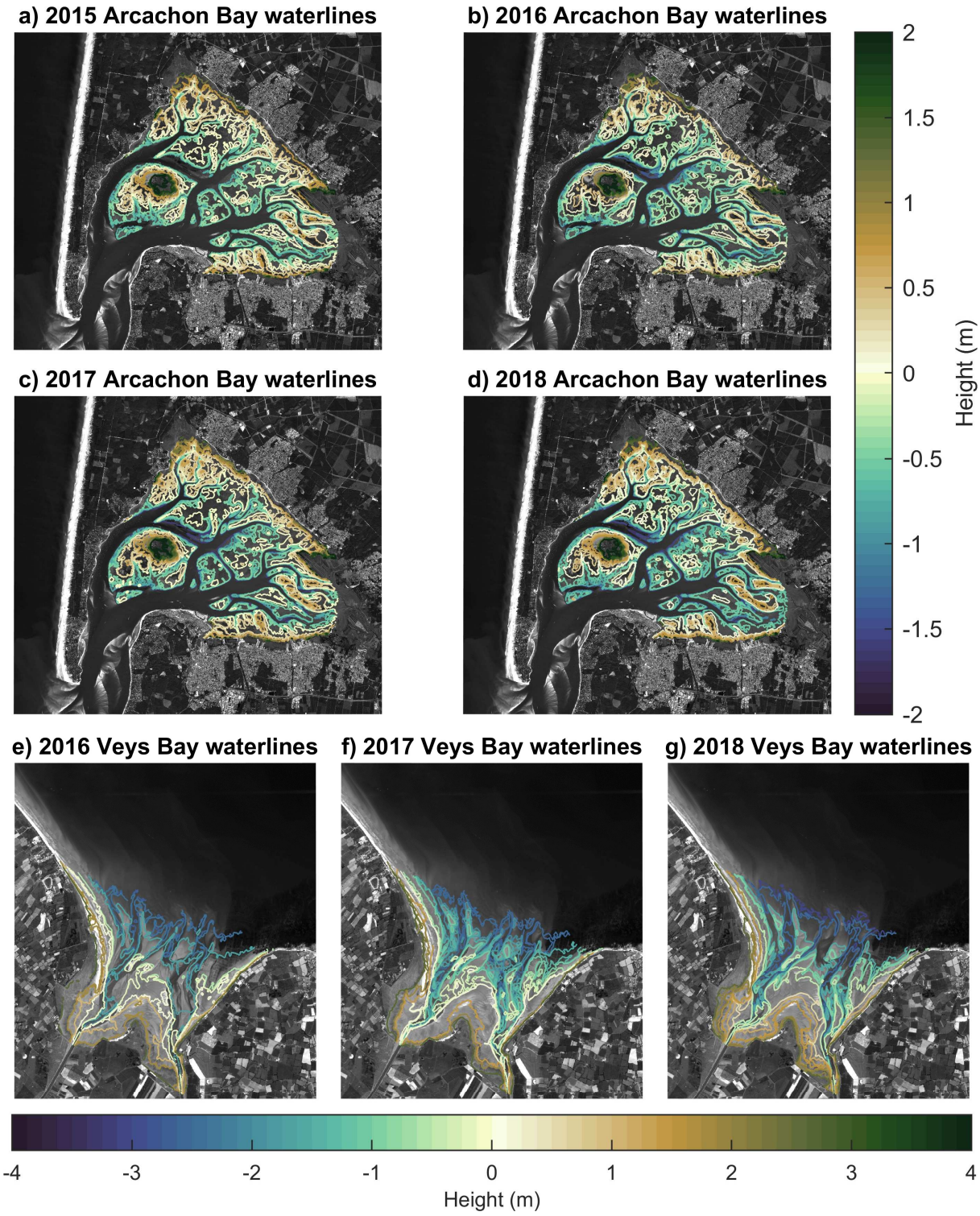

Figure 11. Arcachon Bay assembled waterlines for: (a) 2015; (b) 2016; (c) 2017; (d) 2018, and Bay of Veys assembled waterlines for: (e) 2016; (f) 2017; (g) 2018.

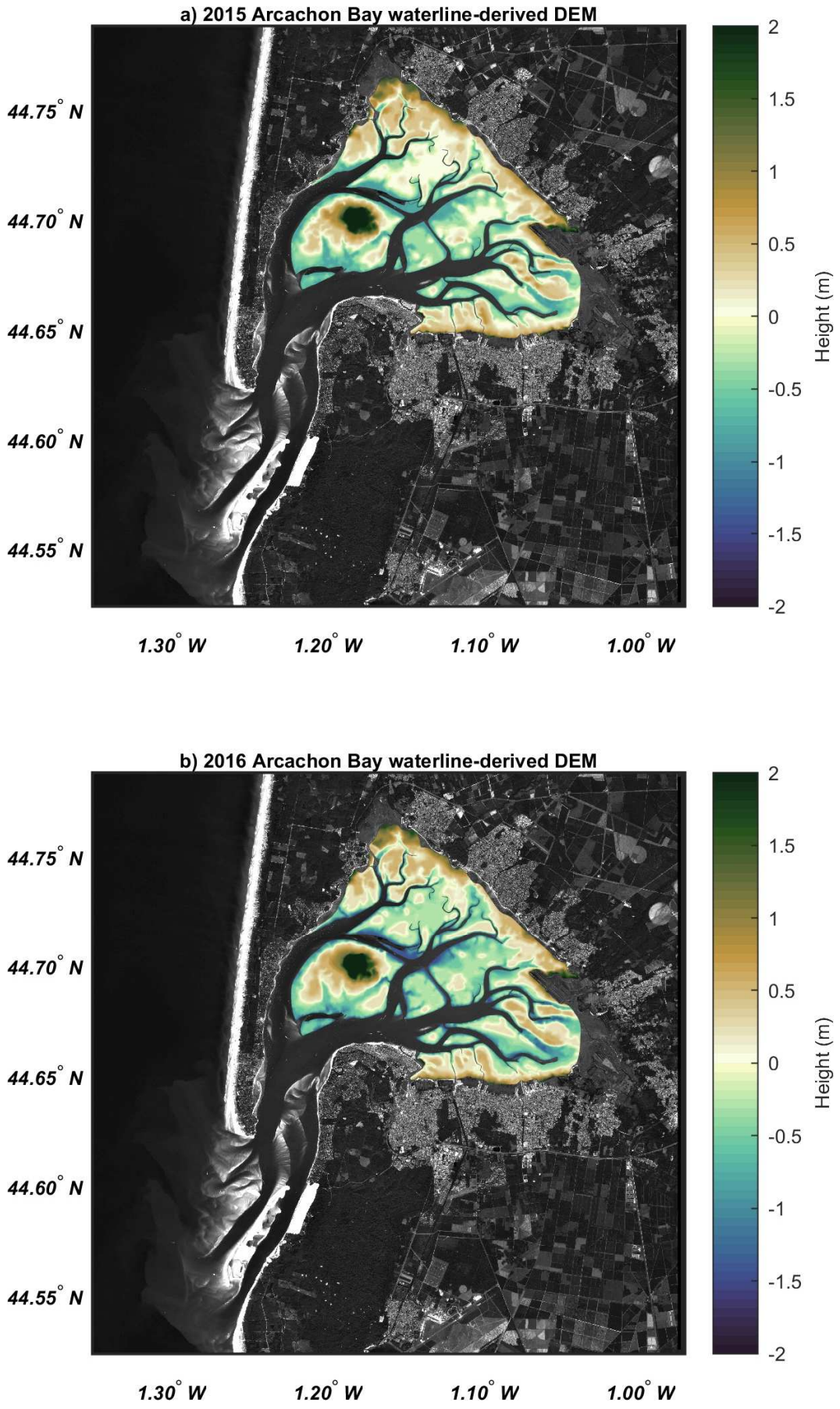

Figure 12. Arcachon Bay waterline-derived DEMs for: (a) 2015; (b) 2016; (c) 2017; and (d) 2018.

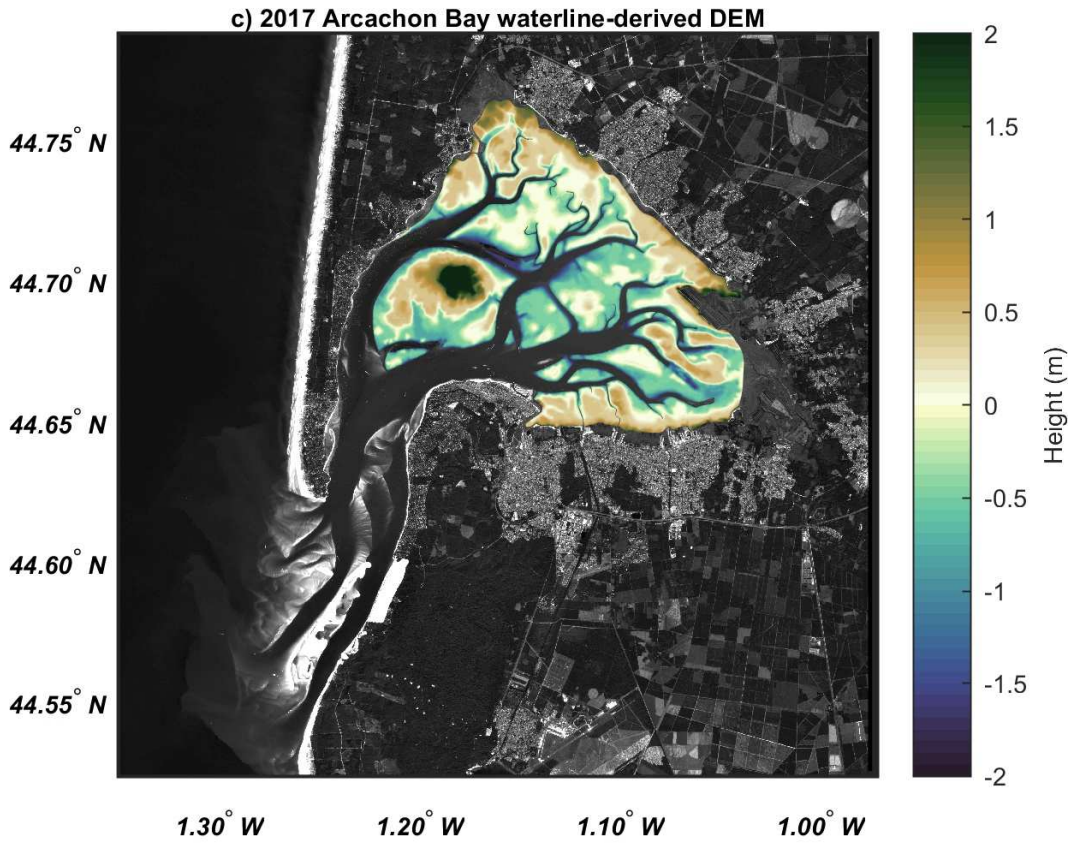

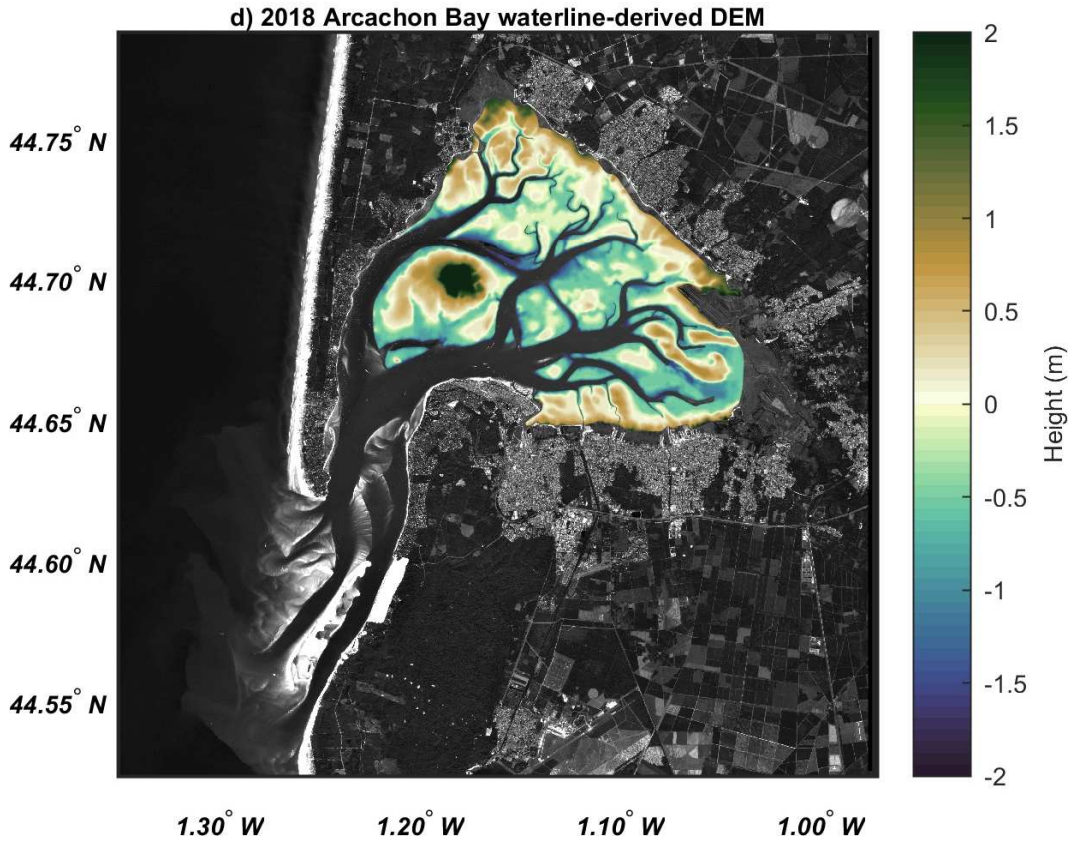

Figure 12. (Continued)

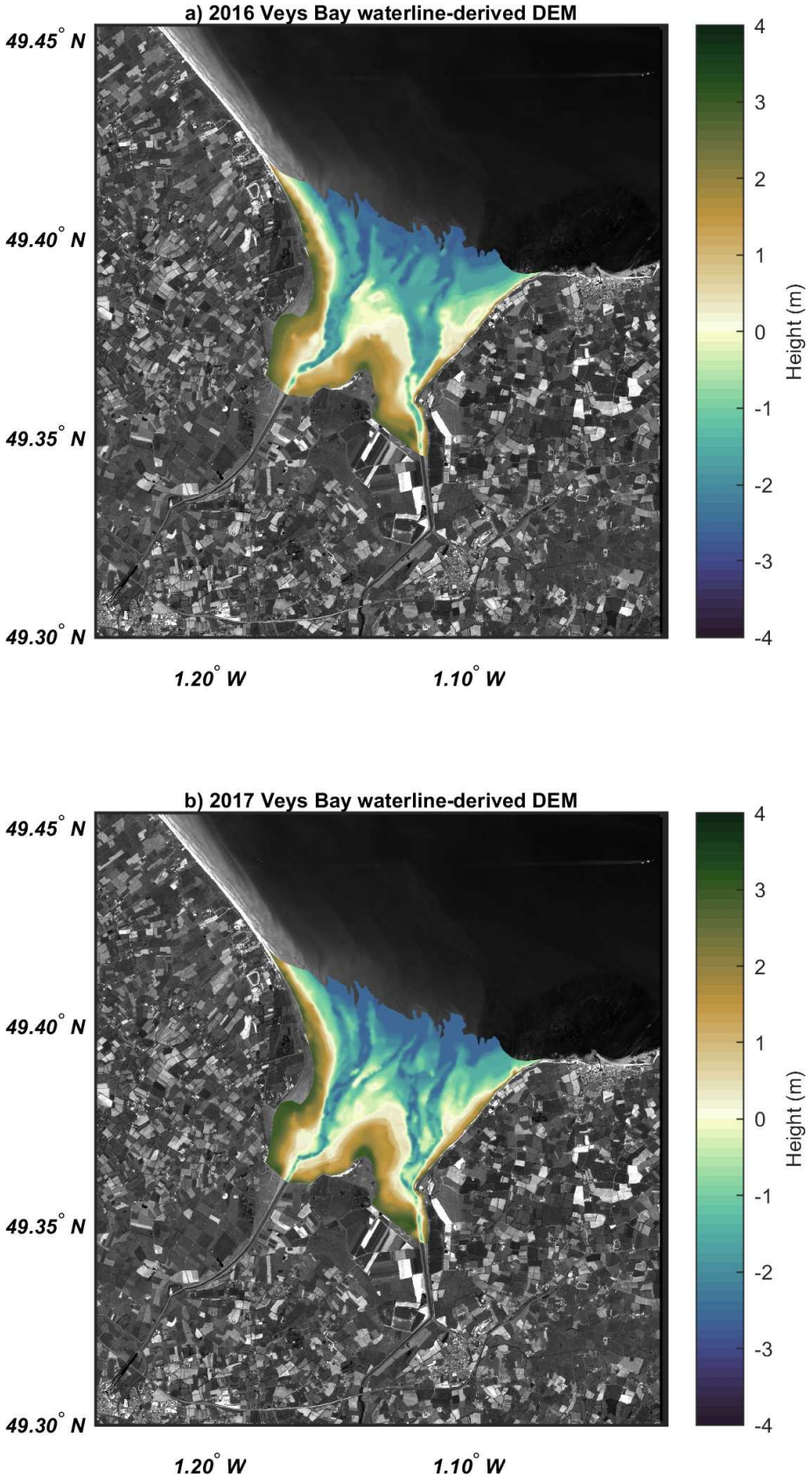

Figure 13. Veys Bay waterline-derived DEMs for: (a) 2016; (b) 2017; and (c) 2018.

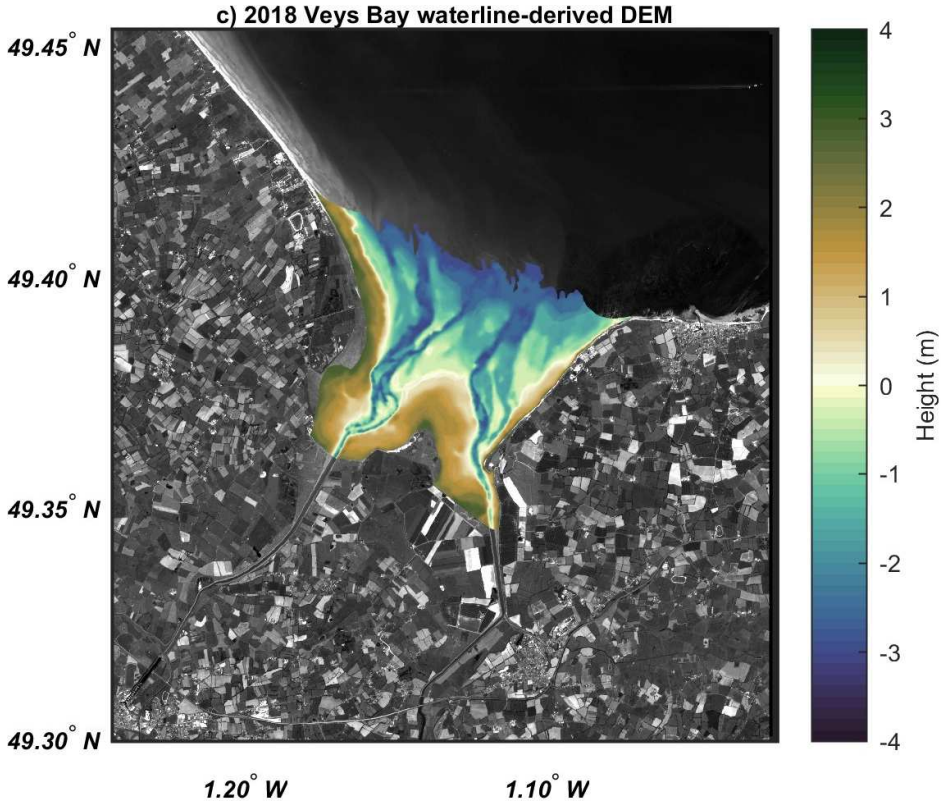

Figure 13. (Continued)

5.4. Monitoring the interannual morpho-sedimentary changes in the intertidal areas

The DEMs of consecutive years were subtracted from one another to generate DoD maps with positive values indicating deposition and negative values indicating erosion. To analyze the change between the overall time period, DoD maps were also generated between the first year and the last year DEMs. The DoD maps are presented in Figure 14 for the Arcachon Bay (Figures 14.a, 14.b, and 14.c) and the Veys Bay (Figures 14.d, 14.e, and 14.f). These differences may result from topographic variations (erosion or deposition) but also from method deficiencies. Therefore, care must be taken when interpreting the pixels with very high differences. The 2015 waterline-derived DEM over the Arcachon Bay was excluded because the lowest waterline detected was considerably higher than the lowest waterlines of other years.

The Arcachon intertidal flats showed an overall stable behavior. The height difference values observed in Figure 14 for the Arcachon Bay are considerably lower than the values obtained for the Veys Bay. For the Arcachon Bay small spots of erosion and deposition distributed over the intertidal area were detected for all years, with two apparent deposition areas observed between 2017 and 2018 at the Eyre Delta. Over the Bay of Veys we observe adjacent erosion and deposition patterns. They are mostly localized along the channels but can also be found at the two sides and in the middle of the intertidal area. This localization over the channels may imply a possible migration of channels between the years.

Considering grid cells with height values between *-LoD* and *LoD* as stable, we computed the stable surface of the intertidal zone for each year along with the surfaces showing erosion and deposition. Eroded, deposited, and net volume changes occurring between the studied years were also computed following the formulation presented in section 4.4. Results are shown in table 2. Net volume changes are higher for 2017/2018 in the case of the Arcachon Bay and the

Bay of Veys. For the whole period (2016/2018), both sites showed significant erosion and deposition volumes (comparing to errors) with total changes showing net losses of 1.12×10^6 m^3 and 0.70×10^6 m^3 for Arcachon and Veys Bays respectively. It should be noted that the lower net changes observed over the Veys Bay is due to the net deposition observed for 2016/2017. However, the amount of the occurring changes was higher for the Bay of Veys despite its smaller intertidal flat area.

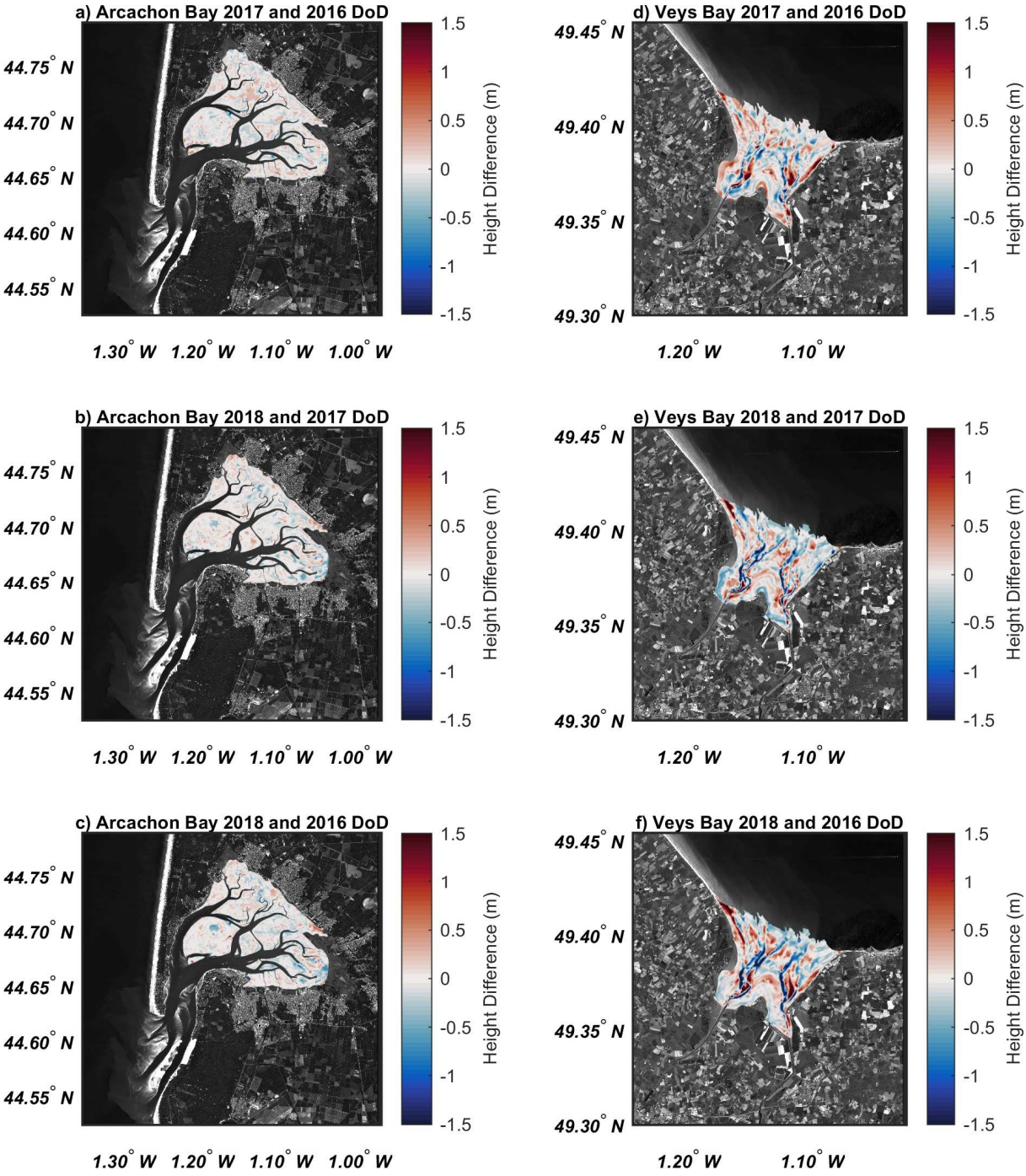

Figure 14. Intertidal flats DEM of Difference (DoD) maps for the Arcachon Bay between a) 2017-2016; b) 2018-2017; c) 2018-2016; and for the Veys Bay between d) 2017-2016; e) 2018-2017; f) 2018-2016.

Table 2. Topographic changes in terms of surface (km^2) and volume (10^6 m^3) between 2016 and 2018 for the Arcachon Bay and the Bay of Veys.

Case	Surface (km^2)			Volume (10^6 m^3)		
	Stable	Eroded	Deposited	Eroded	Deposited	Total
Arcachon 2016/2017	91.30 (98.24%)	1.12 (1.20%)	0.52 (0.56%)	-0.61 ± 0.43	0.24 ± 0.20	-0.37
Arcachon 2017/2018	90.00 (96.85%)	2.27 (2.44%)	0.66 (0.71%)	-1.09 ± 0.87	0.32 ± 0.25	-0.77
Arcachon 2016/2018	89.22 (96.00%)	2.93 (3.15%)	0.79 (0.85%)	-1.54 ± 1.12	0.42 ± 0.30	-1.12
Veys 2016/2017	19.08 (69.51%)	3.51 (12.79%)	4.86 (17.70%)	-2.27 ± 1.19	3.16 ± 1.65	0.90
Veys 2017/2018	17.75 (64.64%)	5.96 (21.70%)	3.75 (13.66%)	-4.11 ± 2.02	2.42 ± 1.27	-1.69
Veys 2016/2018	17.42 (63.44%)	5.16 (18.79%)	4.88 (17.77%)	-4.23 ± 1.75	3.53 ± 1.66	-0.70

6. Discussion

The waterline method has traditionally faced problems with the insufficient number of satellite images acquired during a short period of time, the subjective satellite-image thresholding required in the edge detection process, and the long post-processing (sometimes manual) of the extracted waterlines prior to interpolation. In this study, we demonstrated the ability of the waterline method to generate accurate DEMs in two different intertidal areas located on the French coast (the Arcachon Bay and the Bay of Veys) while trying to overcome the limitations (mentioned above) encountered by this method.

6.1. The number of images

The major approximation made by the waterline method is considering a morphological stability in the intertidal area during the acquisition period of the images. These images acquired during a specified period need also to cover at best the tidal range. Thus, the use of an insufficient number of images or expanding the period of acquisition may lead to inaccuracies. Previous studies generated intertidal DEMs with the waterline method using series of images acquired during periods that spanned over more than one year: 18 and 13images were used by Mason et al. (1999) to generate DEMs for 1991-1994 and 1995-1998 periods respectively; Niedermeier et al. (2005) used 12 images between December 1996 and July 1998 to generate one DEM; Ryu et al. (2008) used 7 images in 16 months (from November 1998 to March 2000) to generate an intertidal DEM; 80 images (from various optical sensors) were used by Wang et al. (2019) to generate an intertidal DEM during a 1 year period in 2010. To our knowledge, the shortest period (5 months) was adopted by Li et al. (2014) (20 images in 2007) and Kang et al. (2017) (18 HJ-1A/B CCD and 3 Landsat TM/OLI images over an exposed area of 2000 km^2 of intertidal flats). Comparing to previous studies, the use of Sentinel-1 and Sentinel-2 data provided a finer and more complete sampling of the tidal range with images acquired during a relatively short period (4 months). Figure 15 shows the coverage of the tidal cycle provided by the Sentinels. It was plotted by computing the average tidal cycle of the acquisition period and by adding the Sentinels' passages relative time (the time of passage during a tidal cycle). Figure 15 shows the improvement of tidal cycle sampling provided by the Sentinels between 2015 and 2018. 2017 and 2018 provide finer sampling of the tidal cycle (comparing to 2015 and 2016) with Sentinel-1A, -1B, -2A, and -2B in orbit. For instance, 80 Sentinel-1 images and 13 cloud free Sentinel-2 images are available for the 2018 June-September period over the Arcachon Bay. However, the total number of 93 images can be considered too high for generating a DEM using the waterline method. The manual selection of images is one of the important issues which limits the complete automatization of

the waterline method. In this study, noisy images and images with similar sea level were automatically removed. However, these two aspects should be further addressed in future studies, especially the determination of the optimal number of waterlines needed (that may depend on a prior knowledge of the intertidal slope) and the estimate of more adequate criteria for images selection in case of redundancy. It should also be noted that the acquisitions made by Sentinel-1 and Sentinel-2 constellations, which provide a huge number of images (every 12 days on the same swath owing to that the study zone can be completely comprised in several swaths), can provide a complete sampling of the tidal range for periods of less than 4 months.

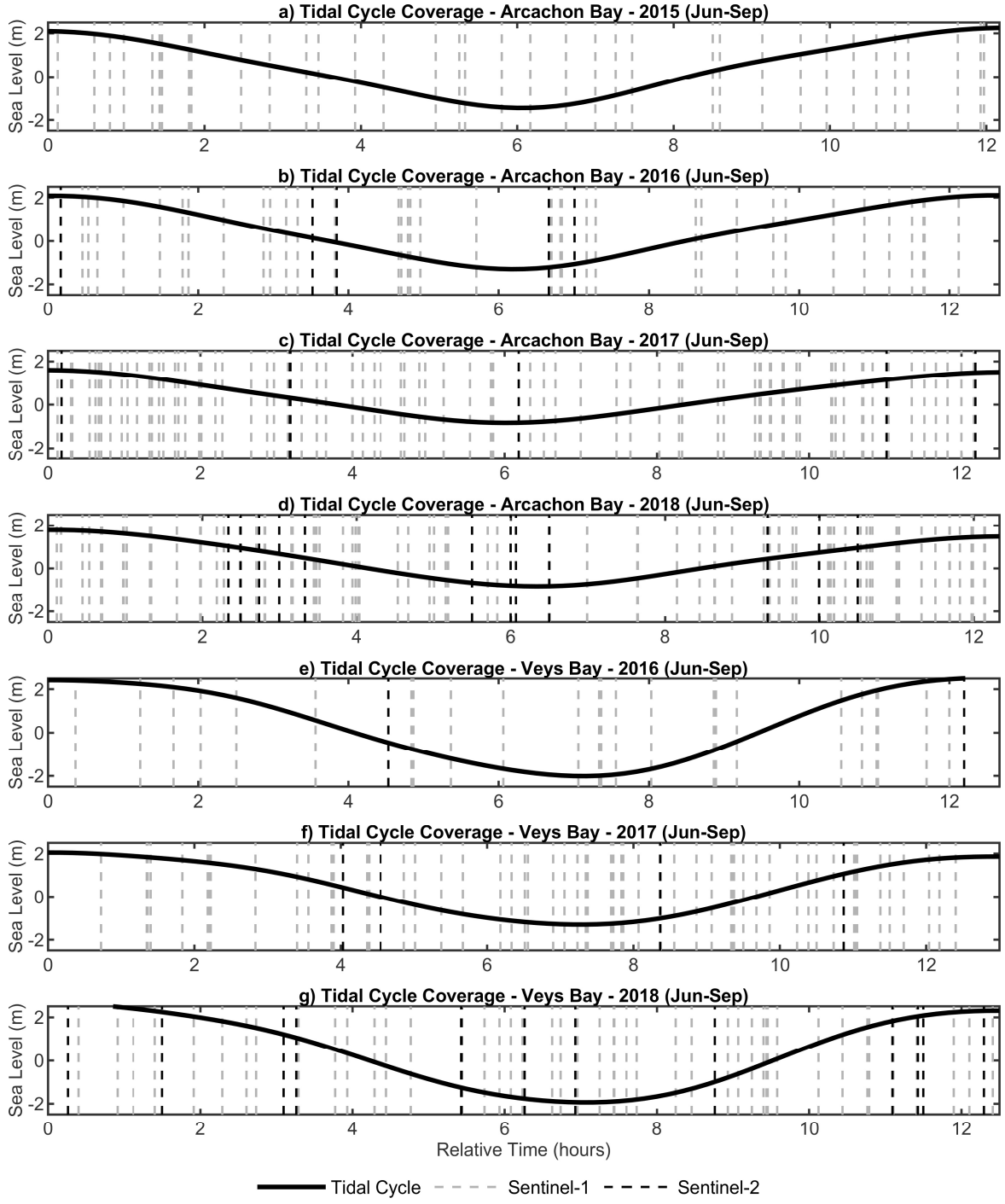

Figure 15. The evolution of the tidal coverage provided by Sentinel-1 and Sentinel-2 for the June-September period between 2015 and 2018 in the Arcachon and Veys Bays.

6.2. Waterlines extraction and post-processing

The first step of the waterline method is to extract the waterlines from the remote sensing images (pre-processed here with SNAP software). An edge detection method based on a combination of k-means segmentation and active contouring was proposed in this study to extract waterlines from Sentinel-1 and Sentinel-2 images. The k-means segmentation technique was employed to overcome two difficulties: the subjective thresholding decisions, and to create closed object to facilitate the post processing of the extracted waterlines. Previous studies that generated intertidal DEMs from SAR images used edge detection methods where a thresholding process was necessary at some point (such as the methods developed by Heygster et al., (2010), Mason and Davenport (1996), and Niedermeier et al. (2000)). These studies performed also a manual post processing of waterlines in order to remove for instance the remaining water ponds, false alarms (false edges), and intersection between waterlines. An automatic post processing was performed in this study thanks to the edge detection method and the closed waterlines provided by it. The manual post-processing may achieve slightly better results comparing to the automatic processing performed in this study. However, the high number of images render this work overwhelming and time consuming. With the unprecedented amount of data available, the automatic post-processing should be always prioritized, and future studies must focus on developing complete automated processing methods. Improvements of the edge detection method might be achieved by using other parameter (such as the backscattering ratio derived from VV and VH polarizations) or by adding another dimension to the k-means clustering (such as the backscattering coefficients derived from the other available polarization).

6.3. Waterlines height assignment and interpolation

Another factor that impacts the accuracy of the generated DEMs is the water level information associated to the extracted waterlines. As mentioned earlier, a waterline is composed of a range of heights and the use of the tide gauge does not take into consideration this reality. However, the use of the complete grid didn't improve the results. This means that either the slope is too low, or the model is incapable of providing very accurate sea level heights over the intertidal area. For interpolation, the major problem encountered was the difference in distance between the lowest waterline from the adopted mask. This can be solved by adding the lowest waterline measured during the whole period to all DEMs or by adding an image acquired at lower tide outside the 4 months period.

6.4. DEMs Accuracy

Figure 16 and Figure 17 present a comparison between the lidar-derived DEM and the waterline-derived DEMs (of all years) over three transects of the Arcachon Bay and the Bay of Veys respectively. MAEs and RMSEs corresponding to these comparisons are listed in Table 3. For the Arcachon Bay, the three 2016 profiles showed lower MAEs (#1: 0.17 m, #2: 0.16 m, #3: 0.14 m) than the one obtained by the complete gridded-DEM (0.19 m) and the estimated accuracy (0.27 m) in section 5.3. A smaller error for profiles is expected because a transect can miss an eventual extensively biased region. However, it shows that a better accuracy can be achieved with more careful processing. The good accuracy provided by this method is also reflected in the MAEs and RMSEs obtained for the 2015 waterline-derived DEM with a MAE reaching 0.13 m for the third transect. Even with this good accuracy, the error is expected to be smaller since the lidar measurements were acquired in 2013. In contrast to transects 1 and 2, small errors barely changing with the years are observed over the third transects crossing the île aux Oiseaux island. This could mean that this area is undergoing less modifications than the rest of the flats.

For the Bay of Veys, lower errors were obtained for the 2017 waterline-derived DEMs as expected. Although, they are higher than the errors observed for the Arcachon Bay. This must be due to the ocean circulation model precision (which is lower than the tide gauge precision). The important morphodynamical changes that can happen in the Veys Bay can also be at the origin of the higher errors.

6.5. Monitoring the interannual morpho-sedimentary changes in the intertidal areas

Repeat DEM surveys and DoD maps are very useful for monitoring morphological changes. However, the inherent uncertainty of the DEMs can considerably affect the computation of volume changes over large areas even for DEMs with very high accuracy (Schimel et al., 2015; Wheaton et al., 2009). In this study we opted for the *LoD* thresholding approach to account for the uncertainty of the estimated volumes of erosion and deposition. The major issue of this technique is the consideration of every change within *-LoD* and *LoD* values as a noise which is not always the case. Therefore, care must be taken when interpreting the estimated volume changes. These changes are considered as a lower bound of the volume displaced at a given confidence interval (which is 68% in this study for $k = 1$) rather than the actual changes (Schimel et al., 2015). Computing volume changes without *LoD* thresholding ($k = 0$) is possible. However, for intertidal flat areas experiencing small height changes comparing to their large surfaces, the summation of the volumetric error over the whole area will yield very large uncertainties. Smaller uncertainties could be obtained by using a standard independent error propagation (i.e., considering each grid-cell has an independent height error), but this is hardly the case for DEMs and can produce statistically invalid uncertainties for volume changes (Schimel et al., 2015).

Considering an LoD thresholding approach, the quantification of sediment surface and volume changes (Table 2) performed here showed that the Arcachon Bay is more stable than the Bay of Veys. 96.00% of stable area was obtained for the Arcachon Bay against 63.44% for the Bay of Veys. The erosion-deposition balance showed a net erosion for all years and for both sites. Between 2016 and 2018 the Arcachon Bay recorded a deficit of sediments of 1.12×10^6 m^3. A net erosion was also obtained for the Bay of Veys with an observed deficit of 0.70×10^6 m^3. We believe that seasonal variation effect is reduced to a minimum because of the use of images acquired during the same season for the DEMs generation.

As we do not have access to sedimentation rate data, we were not able to evaluate the precision of the measured morphological changes. Similar studies performed over different environments showed also net losses. Mason et al. (1999) observed a loss of $(16.1 \pm 4.5) \times 10^6$ m^3 between 1992 and 1997 over the intertidal flats of the Morecambe Bay. Erosion was also observed over the Gomso Bay (Korea) by Ryu et al. (2008) at a rate of -3.1×10^5 m^3/year (- 9 cm over 9 years) between 1991 and 2000. It should be noted that the Morecambe Bay and the Gomso Bay have intertidal flats with surface areas of 350 km^2 and 4,500 km^2 respectively. Comparing to these latter, our two study sites have relatively small area surfaces (115 km^2 and 37 km^2 for Arcachon and Veys Bays respectively). Detecting significant (comparing to the errors) changes over these study sites demonstrates that the methods and datasets used are suited for the monitoring of morphological changes in relatively small-scale environments.

Furthermore, the inspection of Veys profiles (Figure 17) suggests that a detection of channel migrations is possible. For instance, transect 2 shows that the location of the channels detected by the 2017 waterline-derived DEM fits the location detected by the lidar. Whereas, 2016 and 2018 waterline-derived DEMs shows different locations. This can also be seen in Figure 14. The adjacent erosion and deposition patterns may indicate a migration of channels from pixels showing deposition to pixels showing erosion.

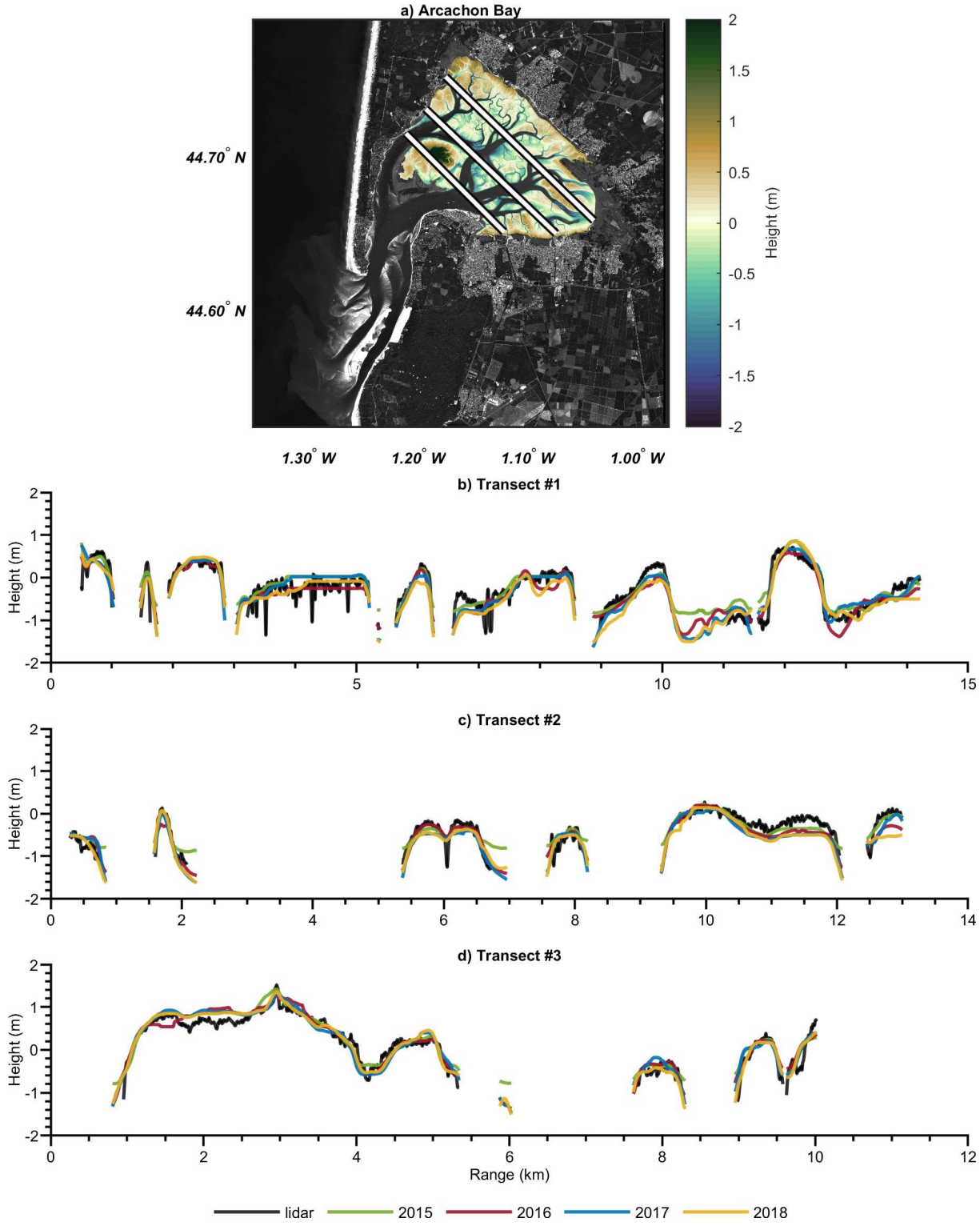

Figure 16. Topography profiles comparison between the lidar-derived DEM and the 2015, 2016, 2017, and 2018 waterline-derived DEMs over the Arcachon Bay along three transects (#1 upper transect; #2 middle transect; #3 lower transect).

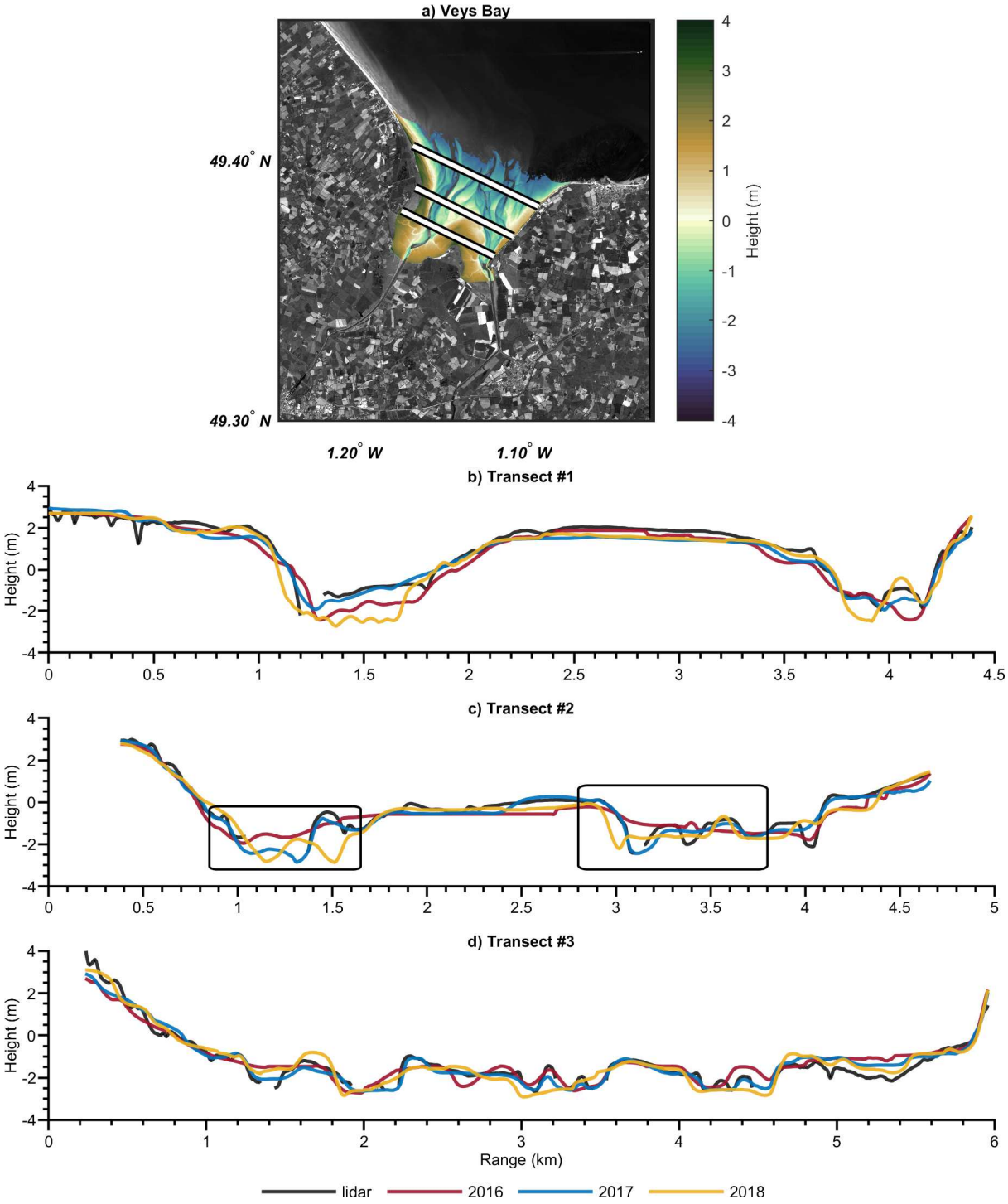

Figure 17. Topography profiles comparison between the lidar-derived DEM and the 2016, 2017, and 2018 waterline-derived DEMs over the Bay of Veys along three transects (#1 lower transect; #2 middle transect; #3 upper transect).

Table 3. Mean Absolute error (MAE) and Root Mean Square error (RMSE) of lidar- and waterline-derived topography profiles of Figures 16 (Arcachon) and 17 (Veys).

	Arcachon						Veys					
	MAE (m)			RMSE (m)			MAE (m)			RMSE (m)		
Year/Transects	#1	#2	#3	#1	#2	#3	#1	#2	#3	#1	#2	#3
2015	0.16	0.14	0.13	0.23	0.18	0.17	x	x	x	x	x	x
2016	0.17	0.16	0.14	0.22	0.19	0.18	0.35	0.37	0.28	0.45	0.51	0.37
2017	0.17	0.18	0.15	0.22	0.22	0.18	0.28	0.23	0.27	0.34	0.35	0.37

2018	0.20	0.20	0.12	0.25	0.25	0.15	0.32	0.37	0.34	0.49	0.58	0.46

7. Conclusions

This study presents a first attempt for intertidal DEM generation of the Arcachon and Veys Bays using the waterline method by analyzing Sentinel-1 and Sentinel-2 images. The major modification to the waterline method comparing to previous studies is the edge detection technique proposed here accompanied by an automatic elimination of noisy SAR images. This edge detection technique of 8 steps based on a combination of k-means segmentation and active contouring provided an accurate, fast, and simple edge detection procedure with faster automatic post-processing of waterlines. A combination of waterlines height assignment approaches and interpolation methods were used to generate the DEMs. The heights were assigned to waterlines using tide gauge records, single point-grid of the ocean-circulation model outputs, and the sea level distribution over the study areas from the gridded model outputs while the interpolation methods used were the IDW and kriging. On these relatively small-scale sites, the best DEMs were generated by combining tide gauge levelling with kriging interpolation. No improvements were observed by taking the surface water slope into account. A vertical accuracy better than 0.27 m and 0.24 m is obtained for Arcachon Bay and Veys Bay respectively (based on gridded-DEMs and profiles comparisons with high accuracy lidar data along with a methodological estimation of the method accuracy). The use of Sentinels data rendered the generated DEMs more reliable due to the high revisit time provided by its two constellations (Sentinel-1 and Sentinel-2) and thus to the finer and complete sampling of the tidal range. The success of the used methodologies and datasets over the two study sites with contrasted characteristics prove their ability to provide accurate and reliable DEMs over similar environments.

A quantitative assessment of morphological changes over the intertidal areas was also performed. Both study sites experienced between 2016 and 2018 a net loss of 1.12×10^6 m^3 for the Arcachon Bay and 0.70×10^6 m^3 for the Bay of Veys, with the Arcachon Bay showing more stable behavior. This study focused on the use of the waterline method with Sentinels images to generate accurate DEMs. However, the significant changes detected by comparing the consecutive DEMs showed that the presented methodologies and datasets are suitable for monitoring the morphological and sedimentary changes of these relatively small-scale intertidal areas. Future work will involve extending of the DEMs time series in order to estimate the morphological changes occurred during the last decade by employing the waterline method using datasets that cover this period. Furthermore, the short period of acquisition (4 months; that can be reduced) might also enable seasonal monitoring of morphological and sedimentary variations. The monitoring of the seasonal and interannual sediment budget of intertidal areas is of great importance for effective management policies.

With more available data and better spatiotemporal resolution, the waterline method can be pushed to its limits. The next-generation wide swath altimetry mission SWOT (Surface Water and Ocean Topography) can generate very useful data to be used by this method. It will provide water masks that can be used as waterlines, and it will measure sea surface height which will render the waterline method independent from ground-based measurements (tide gauges) or hydrodynamic models.

Acknowledgements

This work was supported by the French Space Agency (CNES*; Centre National d'Etudes Spatiales*; and the Normandy Region. The authors would like to thank the three anonymous referees, whose comments improved the manuscript significantly.

8. References

Agardy, T., Alder, J., 2005. Coastal Systems, in: Hassan, R., Scholes, R., Ash, N. (Eds.), Ecosystems and Human Well-Being: Current State and Trends. Island Press, Washington, DC, pp. 513–550.

Allard, J., Chaumillon, E., Féniès, H., 2009. A synthesis of morphological evolutions and Holocene stratigraphy of a wave-dominated estuary: The Arcachon lagoon, SW France. Cont. Shelf Res. 29, 957–969. https://doi.org/10.1016/J.CSR.2008.11.017

Anthony, E.J., Dolique, F., Gardel, A., Gratiot, N., Proisy, C., Polidori, L., 2008. Nearshore intertidal topography and topographic-forcing mechanisms of an Amazon-derived mud bank in French Guiana. Cont. Shelf Res. 28, 813–822. https://doi.org/10.1016/J.CSR.2008.01.003

Arthur, D., Vassilvitskii, S., 2007. k-means++: The advantages of careful seeding, in: Proceedings of the Eighteenth Annual ACM-SIAM Symposium on Discrete Algorithms. Society for Industrial and Applied Mathematics.

Baraille, R., Filatoff, N., 1995. Modèle shallow-water multicouches isopycnal de Miami.

Benveniste, J., Cazenave, A., Vignudelli, S., Fenoglio-Marc, L., Shah, R., Almar, R., Andersen, O., Birol, F., Bonnefond, P., Bouffard, J., Calafat, F., Cardellach, E., Cipollini, P., Le Cozannet, G., Dufau, C., Fernandes, M.J., Frappart, F., Garrison, J., Gommenginger, C., Han, G., Høyer, J.L., Kourafalou, V., Leuliette, E., Li, Z., Loisel, H., Madsen, K.S., Marcos, M., Melet, A., Meyssignac, B., Pascual, A., Passaro, M., Ribó, S., Scharroo, R., Song, Y.T., Speich, S., Wilkin, J., Woodworth, P., Wöppelmann, G., 2019. Requirements for a Coastal Hazards Observing System. Front. Mar. Sci. 6, 348. https://doi.org/10.3389/fmars.2019.00348

Bergsma, E.W.J., Almar, R., 2018. Video-based depth inversion techniques, a method comparison with synthetic cases. Coast. Eng. 138, 199–209. https://doi.org/10.1016/J.COASTALENG.2018.04.025

Blanchet, H., De Montaudouin, X., Chardy, P., Bachelet, G., 2005. Structuring factors and recent changes in subtidal macrozoobenthic communities of a coastal lagoon, Arcachon Bay (France). Estuar. Coast. Shelf Sci. 64, 561–576. https://doi.org/10.1016/j.ecss.2005.03.016

Bleck, R., 2002. An oceanic general circulation model framed in hybrid isopycnic-Cartesian coordinates. Ocean Model. 4, 55–88. https://doi.org/10.1016/S1463-5003(01)00012-9

Bourbigot, M., Johnsen, H., Piantanida, R., 2016. Sentinel-1 Product Definition. Technical Report.

Brasington, J., Rumsby, B.T., McVey, R.A., 2000. Monitoring and modelling morphological change in a braided gravel-bed river using high resolution GPS-based survey. Earth Surf. Process. Landforms 25, 973–990. https://doi.org/10.1002/1096-9837(200008)25:9<973::AID-ESP111>3.0.CO;2-Y

Catalão, J., Nico, G., 2017. Multitemporal Backscattering Logistic Analysis for Intertidal Bathymetry. IEEE Trans. Geosci. Remote Sens. 55, 1066–1073. https://doi.org/10.1109/TGRS.2016.2619067

Chan, T.F., Vese, L.A., 2001. Active Contours Without Edges, IEEE TRANSACTIONS ON IMAGE PROCESSING.

Choi, C., Kim, D., 2018. Optimum Baseline of a Single-Pass In-SAR System to Generate the Best DEM in Tidal Flats. IEEE J. Sel. Top. Appl. Earth Obs. Remote Sens. 11, 919–929.

https://doi.org/10.1109/JSTARS.2018.2795107

Deborde, J., Anschutz, P., Auby, I., Glé, C., Commarieu, M.-V., Maurer, D., Lecroart, P., Abril, G., 2008. Role of tidal pumping on nutrient cycling in a temperate lagoon (Arcachon Bay, France). Mar. Chem. 109, 98–114. https://doi.org/10.1016/j.marchem.2007.12.007

Deroin, J.-P., 2012. Combining ALOS and ERS-2 SAR data for the characterization of tidal flats. Case study from the Baie des Veys, Normandy, France. Int. J. Appl. Earth Obs. Geoinf. 18, 183–194. https://doi.org/10.1016/J.JAG.2012.01.019

Drusch, M., Del Bello, U., Carlier, S., Colin, O., Fernandez, V., Gascon, F., Hoersch, B., Isola, C., Laberinti, P., Martimort, P., Meygret, A., Spoto, F., Sy, O., Marchese, F., Bargellini, P., 2012. Sentinel-2: ESA's Optical High-Resolution Mission for GMES Operational Services. Remote Sens. Environ. 120, 25–36. https://doi.org/10.1016/j.rse.2011.11.026

ESA, 2018. SNAP - ESA Sentinel Application Platform v6.0.0 [WWW Document].

ESA, 2015. SENTINEL-2 User Handbook.

ESA, 2013. Sentinel-1 User Handbook. GMES-S1OP-EOPG-TN-13-0001 [WWW Document].

Fletcher, K., 2012. Sentinel-1: ESA's Radar Observatory Mission for GMES Operational Services (ESA SP-1322/1, March 2012). ESA Communications.

Gao, S., 2019. Geomorphology and sedimentology of tidal flats, in: Coastal Wetlands. Elsevier, pp. 359–381.

Grangeré, K., Ménesguen, A., Lefebvre, S., Bacher, C., Pouvreau, S., 2009. Modelling the influence of environmental factors on the physiological status of the Pacific oyster Crassostrea gigas in an estuarine embayment; The Baie des Veys (France). J. Sea Res. 62, 147–158. https://doi.org/10.1016/J.SEARES.2009.02.002

Heygster, G., Dannenberg, J., Notholt, J., 2010. Topographic Mapping of the German Tidal Flats Analyzing SAR Images With the Waterline Method. IEEE Trans. Geosci. Remote Sens. 48, 1019–1030.

Kang, Y., Ding, X., Xu, F., Zhang, C., Ge, X., 2017. Topographic mapping on large-scale tidal flats with an iterative approach on the waterline method. Estuar. Coast. Shelf Sci. 190, 11–22. https://doi.org/10.1016/J.ECSS.2017.03.024

Lafforgue, M., Gerard, L., Vieillard, C., Breton, M., 2018. Modelling of enterobacterial loads to the Baie des Veys (Normandy, France). Int. J. Hyg. Environ. Health 221, 847–860. https://doi.org/10.1016/J.IJHEH.2018.04.008

Lane, S.N., Westaway, R.M., Murray Hicks, D., 2003. Estimation of erosion and deposition volumes in a large, gravel-bed, braided river using synoptic remote sensing. Earth Surf. Process. Landforms 28, 249–271. https://doi.org/10.1002/esp.483

Lee, J.-S., 1981. Refined filtering of image noise using local statistics. Comput. Graph. Image Process. 15, 380–389. https://doi.org/10.1016/S0146-664X(81)80018-4

Lee, S.-K., Ryu, J.-H., 2017. High-Accuracy Tidal Flat Digital Elevation Model Construction Using TanDEM-X Science Phase Data. IEEE J. Sel. Top. Appl. Earth Obs. Remote Sens. 10, 2713–2724. https://doi.org/10.1109/JSTARS.2017.2656629

Levin, L.A., Boesch, D.F., Covich, A., Dahm, C., Erséus, C., Ewel, K.C., Kneib, R.T., Moldenke, A., Palmer, M.A., Snelgrove, P., Strayer, D., Weslawski, J.M., 2001. The Function of Marine Critical Transition Zones and the Importance of Sediment Biodiversity. Ecosystems 4, 430–451. https://doi.org/10.1007/s10021-001-0021-4

Li, Z., Heygster, G., Notholt, J., 2014. Intertidal Topographic Maps and Morphological Changes in the German Wadden Sea between 1996–1999 and 2006–2009 from the Waterline Method and SAR Images. IEEE J. Sel. Top. Appl. Earth Obs. Remote Sens. 7, 3210–3224. https://doi.org/10.1109/JSTARS.2014.2313062

Liu, Y., Li, M., Zhou, M., Yang, K., Mao, L., 2013. Quantitative Analysis of the Waterline Method for Topographical Mapping of Tidal Flats: A Case Study in the Dongsha Sandbank, China. Remote Sens. 5, 6138–6158. https://doi.org/10.3390/rs5116138

Lohani, B., 1999. Construction of a Digital Elevation Model of the Holderness Coast using the waterline method and Airborne Thematic Mapper data. Int. J. Remote Sens. 20, 593–607. https://doi.org/10.1080/014311699213361

Malenovský, Z., Rott, H., Cihlar, J., Schaepman, M.E., García-Santos, G., Fernandes, R., Berger, M., 2012. Sentinels for science: Potential of Sentinel-1, -2, and -3 missions for scientific observations of ocean, cryosphere, and land. Remote Sens. Environ. 120, 91–101. https://doi.org/10.1016/j.rse.2011.09.026

Mason, D.C., Amin, M., Davenport, I.J., Flather, R.A., Robinson, G.J., Smith, J.A., 1999. Measurement of Recent Intertidal Sediment Transport in Morecambe Bay using the Waterline Method. Estuar. Coast. Shelf Sci. 49, 427–456.

Mason, D.C., Davenport, I.J., 1996. Accurate and efficient determination of the shoreline in ERS-1 SAR images. IEEE Trans. Geosci. Remote Sens. 34, 1243–1253. https://doi.org/10.1109/36.536540

Mason, D.C., Davenport, I.J., Robinson, G.J., Flather, R.A., Mccartney, B.S., 1995. Construction of an inter-tidal digital elevation model by the “water-line” method. Geophys. Res. Lett. 22, 3187–3190.

Mason, D.C., Gurney, C., Kennett, M., 2000. Beach topography mapping - a comparison of techniques. J. Coast. Conserv. 6, 113–124.

Mason, D.C., Scott, T.R., Dance, S.L., 2010. Remote sensing of intertidal morphological change in Morecambe Bay, U.K., between 1991 and 2007. Estuar. Coast. Shelf Sci. 87, 487–496. https://doi.org/10.1016/j.ecss.2010.01.015

Matheron, G., 1963. Principles of geostatistics. Econ. Geol. 58, 1246–1266. https://doi.org/10.2113/gsecongeo.58.8.1246

McFeeters, S.K., 1996. The use of the Normalized Difference Water Index (NDWI) in the delineation of open water features. Int. J. Remote Sens. 17, 1425–1432. https://doi.org/10.1080/01431169608948714

Millennium Ecosystem Assessment, 2005. Ecosystems and Human Well-being: Current State and Trends. Island, Washington DC.

Miranda, N., Meadows, P.J., 2015. Radiometric Calibration of S-1 Level-1 Products Generated by the S-1 IPF, ESA-EOPG-CSCOP-TN-0002. Paris, France.

Murray, N.J., Phinn, S.R., DeWitt, M., Ferrari, R., Johnston, R., Lyons, M.B., Clinton, N., Thau, D., Fuller, R.A., 2019. The global distribution and trajectory of tidal flats. Nature 565, 222–225. https://doi.org/10.1038/s41586-018-0805-8

Nicholls, R.J., Wong, P.P., Burkett, V.R., Codignotto, J.O., Hay, J.E., McLean, R.F., Ragoonaden, C.D., Woodroffe, S., Ragoonaden, S., Woodroffe, C.D., 2007. Coastal systems and low-lying areas., in: Parry, M.L., Canziani, O.F., Palutikof, J.P., van der Linden, P.J., Hanson, C.E. (Eds.), Climate Change 2007: Impacts, Adaptation and Vulnerability. Contribution of Working Group II to the Fourth Assessment Report of the

Intergovernmental Panel on Climate Change. Cambridge University Press, Cambridge, UK, pp. 315–356.

Niedermeier, A., Hoja, D., Lehner, S., 2005. Topography and morphodynamics in the German Bight using SAR and optical remote sensing data. Ocean Dyn. 55, 100–109. https://doi.org/10.1007/s10236-005-0114-2

Niedermeier, A., Romaneeßen, E., Lehner, S., 2000. Detection of Coastlines in SAR Images using Wavelet Methods. IEEE Trans. Geosci. Remote Sens. 38, 2270–2281. https://doi.org/10.1109/36.868884

Pasquet, A., Michaud, H., Aouf, L., Baraille, R., Bru, C., Gouillon, S.C.F., Jourdan, D., Morvan, G., Ohl, P., Paradis, D., 2014. Implémentation d'un nouveau modèle opérationnel de prévision des vagues et surcotes marines, in: XIIIèmes Journées Nationales Génie Côtier – Génie Civil. Dunkerque, pp. 149–158. https://doi.org/10.5150/jngcgc.2014.017

Pebesma, E.J., 2004. Multivariable geostatistics in S: the gstat package. Comput. Geosci. 30, 683–691. https://doi.org/10.1016/J.CAGEO.2004.03.012

Pebesma, E.J., Wesseling, C.G., 1998. Gstat: a program for geostatistical modelling, prediction and simulation. Comput. Geosci. 24, 17–31. https://doi.org/10.1016/S0098-3004(97)00082-4

Plus, M., Dumas, F., Stanisiè Re, J.-Y., Maurer, D., 2009. Hydrodynamic characterization of the Arcachon Bay, using model-derived descriptors. Cont. Shelf Res. 29, 1008–1013. https://doi.org/10.1016/j.csr.2008.12.016

Proença, B., Frappart, F., Lubac, B., Marieu, V., Ygorra, B., Bombrun, L., Michalet, R., Sottolichio, A., Proença, B., Frappart, F., Lubac, B., Marieu, V., Ygorra, B., Bombrun, L., Michalet, R., Sottolichio, A., 2019. Potential of High-Resolution Pléiades Imagery to Monitor Salt Marsh Evolution After Spartina Invasion. Remote Sens. 11, 968. https://doi.org/10.3390/rs11080968

REFMAR, 2012. Marégraphe d'Arcachon Eyrac [WWW Document].

Ryu, J.-H., Kim, C.-H., Lee, Y.-K., Won, J.-S., Chun, S.-S., Lee, S., 2008. Detecting the intertidal morphologic change using satellite data. Estuar. Coast. Shelf Sci. 78, 623–632. https://doi.org/10.1016/J.ECSS.2008.01.020

Salameh, E., Frappart, F., Almar, R., Baptista, P., Heygster, G., Lubac, B., Raucoules, D., Almeida, L.P., Bergsma, E.W.J., Capo, S., De Michele, M., Idier, D., Li, Z., Marieu, V., Poupardin, A., Silva, P.A., Turki, I., Laignel, B., 2019. Monitoring Beach Topography and Nearshore Bathymetry Using Spaceborne Remote Sensing: A Review. Remote Sens. 11, 2212. https://doi.org/10.3390/rs11192212

Salameh, E., Frappart, F., Marieu, V., Spodar, A., Parisot, J.-P., Hanquiez, V., Turki, I., Laignel, B., 2018. Monitoring Sea Level and Topography of Coastal Lagoons Using Satellite Radar Altimetry: The Example of the Arcachon Bay in the Bay of Biscay. Remote Sens. 10, 297. https://doi.org/10.3390/rs10020297

Schimel, A.C.G., Ierodiaconou, D., Hulands, L., Kennedy, D.M., 2015. Accounting for uncertainty in volumes of seabed change measured with repeat multibeam sonar surveys. Cont. Shelf Res. 111, 52–68. https://doi.org/10.1016/J.CSR.2015.10.019

Shepard, D., 1968. A two-dimensional interpolation function for irregularly-spaced data, in: Proceedings of the 1968 23rd ACM National Conference. ACM, New York, USA, pp. 517–524. https://doi.org/10.1145/800186.810616

SHOM-ROLNP, 2018. Lidar Normandie Hauts-de-France (NHDF) 2016-2017 V.20180501

[WWW Document]. URL http://dx.doi.org/10.17183/LIDAR_NHDF_V20180501

SHOM, 2016. Rapport annuel. https://doi.org/10.1111/epp.2605

Showstack, R., 2014. Sentinel Satellites Initiate New Era in Earth Observation. Eos, Trans. Am. Geophys. Union 95, 239–240. https://doi.org/10.1002/2014EO260003

Silveira, M., Heleno, S., 2009. Separation Between Water and Land in SAR Images Using Region-Based Level Sets. IEEE Geosci. Remote Sens. Lett. 6, 471–475. https://doi.org/10.1109/LGRS.2009.2017283

Small, D., Schubert, A., 2008. Guide to ASAR Geocoding (Issue 1.0).

Soares, F., Catalao, J., Nico, G., 2012. Using K-Means and morphological segmentation for intertidal flats recognition, in: 2012 IEEE International Geoscience and Remote Sensing Symposium. IEEE, pp. 764–767. https://doi.org/10.1109/IGARSS.2012.6351452

Timsit, O., Sylvand, B., Lefeuvre, J.-C., 2004. Évolution du macrozoobenthos intertidal de la baie des Veys de 1985 à 2000. C. R. Biol. 327, 51–64. https://doi.org/10.1016/J.CRVI.2003.11.002

Torres, R., Snoeij, P., Geudtner, D., Bibby, D., Davidson, M., Attema, E., Potin, P., Rommen, B., Floury, N., Brown, M., Traver, I.N., Deghaye, P., Duesmann, B., Rosich, B., Miranda, N., Bruno, C., L'Abbate, M., Croci, R., Pietropaolo, A., Huchler, M., Rostan, F., 2012. GMES Sentinel-1 mission. Remote Sens. Environ. 120, 9–24. https://doi.org/10.1016/J.RSE.2011.05.028

Touzi, R., Lopes, A., Bousquet, P., 1988. A Statistical and Geometrical Edge Detector for SAR Images. IEEE Trans. Geosci. Remote Sens. 26, 764–773.

Wang, Y., Liu, Y., Jin, S., Sun, C., Wei, X., 2019. Evolution of the topography of tidal flats and sandbanks along the Jiangsu coast from 1973 to 2016 observed from satellites. ISPRS J. Photogramm. Remote Sens. 150, 27–43. https://doi.org/10.1016/J.ISPRSJPRS.2019.02.001

Weiß, T., 2019. MULTIPLY SAR pre-processing Documentation (Release v0.4).

Wheaton, J.M., Brasington, J., Darby, S.E., Sear, D.A., 2009. Accounting for uncertainty in DEMs from repeat topographic surveys: improved sediment budgets. Earth Surf. Process. Landforms 35, n/a-n/a. https://doi.org/10.1002/esp.1886

Xu, Z., Kim, D., Kim, S.H., Cho, Y.-K., Lee, S.-G., 2016. Estimation of seasonal topographic variation in tidal flats using waterline method: A case study in Gomso and Hampyeong Bay, South Korea. Estuar. Coast. Shelf Sci. 183, 213–220. https://doi.org/10.1016/j.ecss.2016.10.026

Zhao, B., Guo, H., Yan, Y., Wang, Q., Li, B., 2008. A simple waterline approach for tidelands using multi-temporal satellite images: A case study in the Yangtze Delta. Estuar. Coast. Shelf Sci. 77, 134–142. https://doi.org/10.1016/J.ECSS.2007.09.022